Adjoint-based computation of nonlocal eddy viscosity in turbulent channel flow

Jessie Liu [1,*] Florian Schäfer [2] Spencer H. Bryngelson [2,3] Tamer A. Zaki [4] and Ali Mani [1]

[1]*Department of Mechanical Engineering, Stanford University, Stanford, California 94305, USA*
[2]*School of Computational Science & Engineering,*
Georgia Institute of Technology, Atlanta, Georgia 30332, USA
[3]*Daniel Guggenheim School of Aerospace Engineering,*
Georgia Institute of Technology, Atlanta, Georgia 30332, USA
[4]*Department of Mechanical Engineering, Johns Hopkins University, Baltimore, Maryland 21218, USA*

Reynolds-averaged Navier–Stokes (RANS) closure operators are generally nonlocal and anisotropic for many flows, including wall-bounded turbulence. The macroscopic forcing method (MFM) and Green's function-based approaches examine these effects using forced direct numerical simulations. For these approaches, the number of simulations required to compute the nonlocal and anisotropic eddy viscosity is equal to the number of degrees of freedom in the averaged space. We reduce the computational cost by introducing an adjoint-based formulation of MFM to obtain the nonlocal and anisotropic eddy viscosity at any Reynolds stress location using a single simulation. We then quantify the streamwise and wall-normal nonlocal eddy viscosity at near-wall locations in turbulent channel flow at $\mathrm{Re}_\tau = 180$. We demonstrate that the upstream nonlocality is not fully described by Lagrangian transport. We also quantify the significant differences in the upstream non-locality between various components of the eddy viscosity tensor. Our results can be used to guide closure modeling, including the lengthscales and timescales used in Reynolds stress models.

I. INTRODUCTION

Reynolds-averaged Navier–Stokes (RANS) models are widely used to simulate turbulent flows where direct numerical simulation (DNS) of the governing equations may be computationally cost-prohibitive. The flow variables are Reynolds decomposed into mean and fluctuating components, and the RANS equations govern the mean fields [1]. However, an unclosed term involves the product of velocity fluctuations, commonly known as the Reynolds stress tensor. Further attempts to derive an exact evolution equation for the Reynolds stresses result in more unclosed terms, and hence, the Reynolds stresses are typically modeled [2–4].

Recent works by Hamba [5] and Park and Mani [6] have computed exact closure operators for Reynolds stresses. These closure operators can further be written in terms of generalized eddy viscosities that are nonlocal in space and time and anisotropic [5]. The closure operators are exact in that substituting these operators back into the RANS equations results in DNS mean quantities. Naturally, the operators are problem-dependent, but they can be used to inform current RANS models of deficiencies in their eddy viscosity approximations and regions of sensitivity to the mean velocity gradient.

---

*Contact author: jeliu@stanford.edu

Kraichnan [7] derived an exact nonlocal and anisotropic expression for the Reynolds stress tensor using a Green's function. Hamba [5] modified the expression to be feasible for numerical implementation. Hamba [5] used the Green's function solution to a linearized formulation of the velocity fluctuation equation, where the mean velocity gradient is treated as the source and the velocity fluctuation is treated as the response. The generalized nonlocal and anisotropic eddy viscosity is then formulated using Green's functions and velocity fluctuations. Because this approach needs the Green's function solution at each location in the averaged space, using a separate simulation for each location, computing the generalized eddy viscosity requires as many DNSs as degrees of freedom in the averaged space. Mani and Park [8] developed the macroscopic forcing method (MFM), a linear-algebra-based method for numerically obtaining closure operators. In MFM, one examines the closure operator by applying an appropriate forcing (not necessarily a Dirac δ function) to the governing equations and measures the averaged response. While MFM can obtain the exact generalized eddy viscosity when used as a brute-force approach similar to Hamba's approach [5], MFM can also obtain moments of the eddy viscosity using one simulation per desired moment. Liu *et al.* [9] showed how to use the limited information from a few low-order moments to model the eddy viscosity. The resulting eddy viscosity is nonlocal and matches the measured low-order moments, while the shape of its kernel approximately resembles the true kernel.

For many applications, the exact eddy viscosity may be desired only within subregions of the domain where RANS models are particularly inaccurate, such as in regions of flow separation [10–12]. The generalized eddy viscosity at such locations can inform RANS models of the sensitivity of the Reynolds stresses at those locations to the mean velocity gradient at all locations. However, brute-force approaches [5,8] are cost-prohibitive and compute the generalized eddy viscosity for the entire domain, entailing as many simulations as degrees of freedom in the averaged space.

We herein develop an adjoint-based method to compute the generalized eddy viscosity at a specific physical location using one simulation rather than an expensive brute-force approach. We then use the adjoint-based method to quantify the two-dimensional (2D) streamwise and wall-normal nonlocal eddy viscosity in turbulent channel flow at near-wall locations. Due to its many degrees of freedom, obtaining this eddy viscosity with a brute-force approach was previously too cost-prohibitive. Figure 1 illustrates computing the one-dimensional (1D) wall-normal eddy viscosity for a canonical turbulent channel flow using brute force and our proposed approach. Averaging is taken in time and over homogeneous streamwise and spanwise directions, such that the eddy viscosity is only a function of the wall-normal direction. The mean velocity gradient is specified as an impulse at a wall-normal location (Fig. 1; blue plane), and a forced DNS is used to examine the Reynolds stress response. One such brute-force simulation characterizes how the mean velocity gradient at a specific location influences the Reynolds stress at all wall-normal locations, forming a column of the discretized eddy viscosity. The proposed adjoint-based approach characterizes how the Reynolds stress at a specific location (Fig. 1; orange plane) is influenced by the mean velocity gradient at all wall-normal locations, forming a row of the discretized eddy viscosity and is more physically relevant. Computing a row using the brute-force approach would have required obtaining all columns of the eddy viscosity, using a separate simulation for each column. For the 1D wall-normal eddy viscosity, the number of simulations needed is equal to the number of mesh points in the wall-normal direction. For the 2D streamwise and wall-normal eddy viscosity, the number of simulations needed is the number of mesh points in the streamwise and wall-normal directions, and hence, was previously too cost-prohibitive to investigate with a brute-force approach. While this work focuses on Reynolds stress closures, our adjoint-based approach applies to more general closures, including for scalar fluxes [13], compressible flows [4,14], and disperse multiphase flows [15].

The adjoint-based formulation in this work can also aid in efficiently computing the eddy viscosity for the entire domain. Bryngelson *et al.* [16] revealed hidden sparsity in the discretized eddy viscosity to establish fast MFM, substantially reducing the number of simulations required to obtain the generalized eddy viscosity. This work's adjoint-based method enables a straightforward and computationally efficient way of recovering the operator rows (and columns) required for the
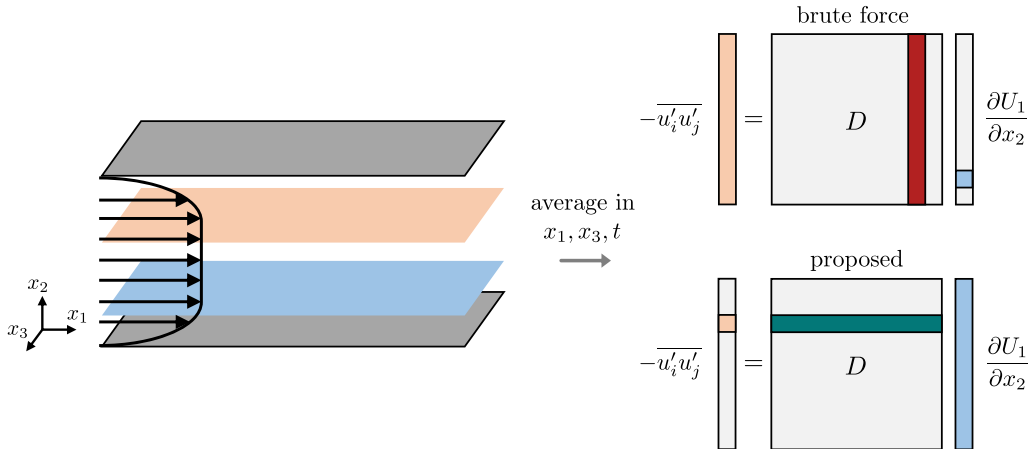
FIG. 1. MFM illustration for obtaining the 1D wall-normal eddy viscosity for channel flow. With a brute-force approach, the mean velocity gradient, $\partial U_1 / \partial x_2$, is specified as an impulse at a wall-normal location (blue plane), which corresponds to activating one element of the mean velocity gradient vector as shown in the top right of the figure. A forced DNS is used to measure the Reynolds stress response, $-\overline{u_i' u_j'}$ at all x_2 locations. This recovers one column of the discretized eddy viscosity, D, and must be repeated for all mean velocity gradient locations. The proposed adjoint MFM obtains a more physically relevant row of D, relating the Reynolds stress at one location (orange plane) to the mean velocity gradient at all wall-normal locations as shown in the bottom right of the figure.

LU recovery algorithm underlying fast MFM [16,17]. Through selective forcing, such that the output of each simulation contains information about multiple rows and columns of the discretized eddy viscosity, Bryngelson *et al.* [16] reconstruct the discretized eddy viscosity for the entire domain using substantially fewer simulations than a brute-force approach.

Using the adjoint-based MFM formulation developed in this work, we investigate the 2D streamwise and wall-normal nonlocal eddy viscosity in turbulent channel flow at several near-wall locations at $\mathrm{Re}_\tau = 180$. Hamba [13] computed the streamwise and wall-normal nonlocal eddy diffusivity for passive scalar transport in turbulent channel flow at $\mathrm{Re}_\tau = 180$ using a brute-force approach. Here, we investigate momentum transport. Prior works [6,18] investigated the 1D wall-normal nonlocal eddy viscosity in turbulent channel flow at $\mathrm{Re}_\tau = 180$ using brute-force approaches. This work extends the focus to nonlocality in the streamwise direction. While the streamwise direction is homogeneous in turbulent channel flow, we use the eddy viscosity to understand nonlocal effects in wall-bounded flows by considering turbulent channel flow as a canonical test case.

In Sec. II, we define the generalized eddy viscosity and illustrate the cost of obtaining it using MFM. In Sec. III, we develop adjoint MFM for obtaining the eddy viscosity for a specific Reynolds stress location. In Sec. IV, we discuss the numerical details of the simulations. In Sec. V, we compare MFM and adjoint MFM for computing the 1D wall-normal nonlocal eddy viscosity in turbulent channel flow at $\mathrm{Re}_\tau = 180$. We then use adjoint MFM to obtain the 2D streamwise and wall-normal nonlocal eddy viscosity at several near-wall locations. We also characterize the streamwise nonlocality lengthscale, examine the anisotropy in the eddy viscosity tensor, and discuss the physical implications for the lengthscales and timescales used in Reynolds stress transport models.

II. PROBLEM FORMULATION

Many RANS models [2–4] use the Boussinesq approximation [19] in which there are two underlying assumptions: (1) The lengthscales and timescales of the underlying velocity fluctuations

are much smaller than that of the mean velocity fields, and hence the mixing by the turbulent fluctuations is assumed to be local; (2) the mixing by the underlying fluctuations is assumed to be isotropic; hence, the Reynolds stress tensor and mean strain rate tensor are aligned. Under the Boussinesq approximation, an analogy is drawn to Brownian motion, for which random molecular mixing is modeled using a diffusive flux, and the Reynolds stress is modeled in terms of a scalar eddy viscosity and the mean velocity gradient. However, for turbulent flows, the underlying assumptions of the Boussinesq approximation are often invalid [20].

Hamba [5] developed an exact closure for the Reynolds stress, $-\overline{u_i' u_j'}$, using a generalized eddy viscosity:

$$-\overline{u_i' u_j'}(\mathbf{x}, t) = \int_{\mathbf{y}, \tau} D_{ijkl}(\mathbf{x}, \mathbf{y}, t, \tau) \frac{\partial U_l}{\partial x_k}\bigg|_{\mathbf{y}, \tau} d\mathbf{y} d\tau, \tag{1}$$

where $D_{ijkl}(\mathbf{x}, \mathbf{y}, t, \tau)$ is the nonlocal and anisotropic eddy viscosity kernel, and U_l is the mean velocity. The eddy viscosity is (1) spatiotemporally nonlocal in that the Reynolds stress depends on the mean velocity gradient at all points in space and time and (2) anisotropic in that the Reynolds stress tensor and velocity gradient tensor are not necessarily aligned.

Hamba [5] and Park and Mani [6] computed the wall-normal nonlocal eddy viscosity kernel for turbulent channel flow at $\mathrm{Re}_\tau = 180$. Hamba [5] used the Green's function solution to a linearized equation for the velocity fluctuations. Park and Mani [6] used inverse MFM (IMFM), where forcing is added to the governing equations to maintain a pre-specified mean velocity gradient. For computing the generalized eddy viscosity, Liu *et al.* [9] showed that the two approaches are equivalent. However, Hamba [5] further performed averaging of the components of D_{ijkl} to enforce symmetry in the eddy viscosity tensor, e.g., $(D_{2121} + D_{1221})/2$, whereas Park and Mani [6] did not. We discuss IMFM in this work, although one can also use the approach of Hamba [5].

Park and Mani [6] simultaneously solve the incompressible Navier–Stokes equations:

$$\frac{\partial u_i}{\partial t} + \frac{\partial u_j u_i}{\partial x_j} = -\frac{\partial p}{\partial x_i} + \frac{1}{\mathrm{Re}} \frac{\partial^2 u_i}{\partial x_j \partial x_j} + r_i, \tag{2a}$$

$$\frac{\partial u_i}{\partial x_i} = 0, \tag{2b}$$

where Re is the Reynolds number, p is the fluctuating pressure, and r_i is a body force, which for turbulent channel flow is the nondimensionalized mean pressure gradient, $r_i = (1, 0, 0)$, and the generalized momentum transport (GMT) equations:

$$\frac{\partial v_i}{\partial t} + \frac{\partial u_j v_i}{\partial x_j} = -\frac{\partial q}{\partial x_i} + \frac{1}{\mathrm{Re}} \frac{\partial^2 v_i}{\partial x_j \partial x_j} + s_i, \tag{3a}$$

$$\frac{\partial v_i}{\partial x_i} = 0, \tag{3b}$$

where u_j is the advection velocity obtained from the Navier–Stokes equations, v_i is a transported vector field, q is a generalized pressure to ensure that v_i is solenoidal, and s_i is the IMFM forcing (and must satisfy $s_i = \overline{s_i}$). In this formulation, the eddy viscosity is

$$-\overline{u_i' v_j'}(\mathbf{x}, t) = \int_{\mathbf{y}, \tau} D_{ijkl}(\mathbf{x}, \mathbf{y}, t, \tau) \frac{\partial V_l}{\partial x_k}\bigg|_{\mathbf{y}, \tau} d\mathbf{y} d\tau. \tag{4}$$

The relationship between the closure operator in Eqs. (4) and (1) is further discussed in Mani and Park [8] and Hamba [5]. Mani and Park [8] showed that in the absence of forcing, the vector field v_i in the GMT equations in Eqs. (3a) and (3b) exponentially converges to the DNS velocity field u_i. Moreover, Park and Mani [6] numerically showed that substitution of the measured eddy viscosity kernel, $D_{ijkl}(\mathbf{x}, \mathbf{y}, t, \tau)$, from Eq. (4) into Eq. (1) with the DNS mean velocity gradient results in Reynolds stresses identical to DNS for turbulent channel flow.
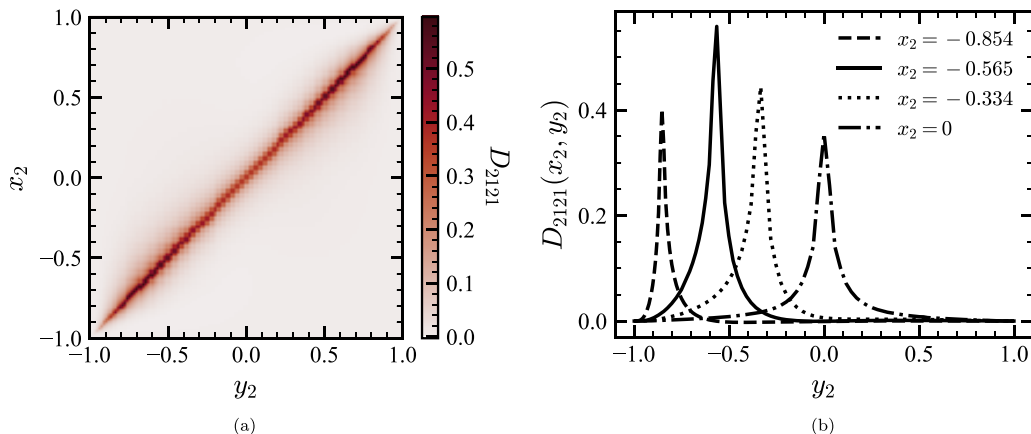
FIG. 2. (a) $D_{2121}(x_2, y_2)$ component of the generalized eddy viscosity for a turbulent channel flow at $\text{Re}_\tau = 180$. $D_{2121}(x_2, y_2)$ represents the dependence of the shear component of the Reynolds stress, $-\overline{u_2' v_1'}(x_2)$, on $\partial V_1/\partial x_2|_{y_2}$. Reproduced from Park and Mani [6] with author permission. (b) $D_{2121}(x_2, y_2)$ for x_2 as labeled. Uses data from Park and Mani [6].

As a 1D example, Fig. 2(a) shows the $D_{2121}(x_2, y_2)$ component of the wall-normal nonlocal eddy viscosity kernel for statistically stationary turbulent channel flow at $\text{Re}_\tau = 180$ reproduced from Park and Mani [6], where

$$-\overline{u_2' v_1'}(x_2) = \int D_{2121}(x_2, y_2) \frac{\partial V_1}{\partial x_2}\bigg|_{y_2} dy_2. \tag{5}$$

Averaging is taken in time and in the homogeneous streamwise (x_1) and spanwise (x_3) directions. The $D_{2121}(x_2, y_2)$ component represents the dependence of the shear component of the Reynolds stress, $-\overline{u_2' v_1'}(x_2)$, on the mean velocity gradient at all locations, $\partial V_1/\partial x_2|_{y_2}$. To compute the eddy viscosity kernel, Park and Mani [6] used the IMFM forcing to maintain the mean velocity gradient, $\partial V_1/\partial x_2$, as a Dirac δ function. At each time step, the governing equation is first time advanced without the forcing to solve for an intermediate velocity field, and then the forcing is added in a correction step to ensure the velocity field at the next time step has the requisite mean velocity as discussed in Refs. [8,16]. In discretized form, $\mathbf{b} = \mathbf{A}\mathbf{v}$, where $\mathbf{b} = -\overline{u_2' v_1'}$ is a $N \times 1$ vector, $\mathbf{A} = D_{2121}$ is a $N \times N$ matrix, $\mathbf{v} = \partial V_1/\partial x_2$ is a $N \times 1$ vector, and N is the number of degrees of freedom in the averaged space (number of mesh points in x_2). Using IMFM to specify the velocity gradient as $\mathbf{v} = [1\ 0 \ldots 0]^\top$ (a discrete Dirac δ function) and post-processing the resulting $-\overline{u_2' v_1'}$ from a simulation of the Navier–Stokes equations (2a) and (2b) and GMT equations (3a) and (3b) leads to the first column of $\mathbf{A}$. Specifying $\mathbf{v} = [0\ 1 \ldots 0]^\top$ leads to the second column, and so forth. Thus, obtaining the generalized eddy viscosity using IMFM, or equivalently Hamba's approach [5] here, requires as many simulations as degrees of freedom in the averaged space. In the case of Park and Mani [6], 144 simulations were required to produce the eddy viscosity shown in Fig. 2(a). Each simulation solves the incompressible Navier–Stokes and GMT equations; hence, the total cost is equivalent to 288 DNSs.

Each simulation obtains a column of D_{ijkl}, but the rows of D_{ijkl} are more useful from a physical perspective. The rows give the dependence of the Reynolds stresses at a given location on the mean velocity gradient at all locations. The rows give information about the importance of nonlocality and regions of mean velocity gradient sensitivity. Moreover, the rows of D_{ijkl} are generally not identical to the columns. For example, from Fig. 2(a) it may seem that $D_{2121}(x_2 = -0.565, y_2)$ is symmetric and equal to $D_{2121}(x_2, y_2 = -0.565)$. Figure 3 shows clear differences between a row of D_{2121} at $x_2 = -0.565$ and a column at the same location. We first address the need for a method for obtaining
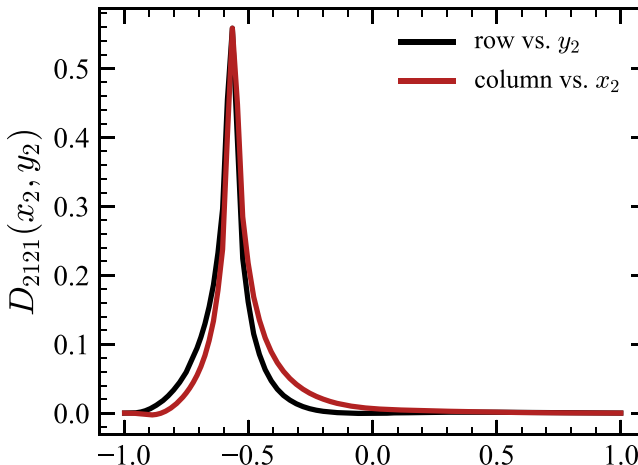
FIG. 3. A row of D_{2121} at $x_2 = -0.565$, i.e., $D_{2121}(x_2 = -0.565, y_2)$ and the corresponding column, $D_{2121}(x_2, y_2 = -0.565)$, which shows that $D_{2121}(x_2, y_2)$ is not symmetric (data from Park and Mani [6] with author permission).

targeted rows of the generalized eddy viscosity without performing a brute-force computation of all columns of the eddy viscosity by developing adjoint MFM. We show verification of adjoint MFM by comparing the 1D wall-normal eddy viscosity at $x_2 = -0.565$ with Park and Mani [6]. We then use adjoint MFM to quantify the 2D streamwise and wall-normal eddy viscosity at near-wall locations.

III. ADJOINT MFM

We develop a method for obtaining a specific row of the generalized eddy viscosity, representing the nonlocal dependence of the Reynolds stress at a specific point on mean velocity gradients at all points in space/time, using an adjoint formulation of the GMT equations. To simplify the exposition, we derive adjoint MFM in the discrete setting in terms of linear operators represented by finite-dimensional matrices and using the Euclidean inner product. In this case, taking the adjoint of a linear operator amounts to taking the conjugate transpose of its matrix representation. Our derivation extends to the continuous case by replacing matrices with linear operators on function spaces and transposes with adjoints with respect to the energy inner product. We use D_{ijkl} to denote the eddy viscosity discretely and $D_{ijkl}(\mathbf{x}, \mathbf{y})$ to denote the eddy viscosity kernel continuously.

The generalized eddy viscosity is part of a linear operator, $\overline{\mathcal{L}}$, that acts on the mean variables, V, such that the mean equation is

$$\overline{\mathcal{L}} V = 0. \tag{6}$$

After discretization, V is a finite-dimensional vector of all mean velocity components and pressure, $V = [V_j \, Q]^{\top}$, and $\overline{\mathcal{L}}$ includes closed operators and the Reynolds stress closure operator, $\overline{\mathcal{L}}'$, formed by the eddy viscosity, written in block form as

$$\overline{\mathcal{L}} = \begin{bmatrix} \frac{\partial}{\partial t} + U_i \frac{\partial}{\partial x_i} - \frac{1}{\mathrm{Re}} \frac{\partial^2}{\partial x_i \partial x_i} + \overline{\mathcal{L}}' & \frac{\partial}{\partial x_j} \\ \frac{\partial}{\partial x_j} & 0 \end{bmatrix}, \tag{7}$$

where the partial derivatives are discretized operators, and where

$$\overline{\mathcal{L}}' V = \frac{\partial}{\partial x_i} \overline{u_i' v_j'} = -\frac{\partial}{\partial x_i} D_{ijkl} \frac{\partial V_l}{\partial x_k}. \tag{8}$$

Similarly, the governing equations, e.g., the GMT equations (3a) and (3b), can be discretized as

$$\mathcal{L}v = 0. \tag{9}$$

Mani and Park [8] show that

$$\overline{\mathcal{L}} = (P\mathcal{L}^{-1}E)^{-1}, \tag{10}$$

where P is a projection operator such that $V = Pv$ and E is an extension operator such that $E = nP^{\top}$, where n is the number of points used for averaging. The derivation of (10) is shown in Appendix A. In practice, most problems have many degrees of freedom, and $\mathcal{L}$ is expensive to invert directly. IMFM takes advantage of computational fluid dynamics solvers to compute Eq. (10) column-by-column by considering the forced mean equation:

$$\overline{\mathcal{L}}V = \bar{s}, \tag{11}$$

which can be computationally assessed by forcing the DNS equation:

$$\mathcal{L}v = s, \tag{12}$$

where $s = E\bar{s}$ (the extension operator is added since s and $\bar{s}$ may have different dimensions as discussed in Appendix A). Linear algebraically speaking, the $\bar{s}$ obtained for a given V is the matrix-vector product of $\overline{\mathcal{L}}$ with V. IMFM allows computing individual columns of $\overline{\mathcal{L}}$ by choosing V, e.g., as $V = [1\ 0\ldots 0]^{\top}$ to obtain the first column of $\overline{\mathcal{L}}$. Once $\overline{\mathcal{L}}$ is obtained, one can derive $\overline{\mathcal{L}}'$ by subtracting the closed temporal and spatial derivatives in Eq. (7), and inverting the spatial derivatives:

$$D_{ijkl} = -\left[\frac{\partial}{\partial x_i}\right]^{-1}\overline{\mathcal{L}}'\left[\frac{\partial}{\partial x_k}\right]^{-1}. \tag{13}$$

In 1D problems, it is possible to compute D_{ijkl} from Eq. (13). To circumvent the ill-posedness of inverting multi-dimensional divergence operators, Park and Mani [6] instead compute the generalized eddy viscosity directly from Eq. (8),

$$-\overline{u_i'v_j'} = D_{ijkl}\frac{\partial V_l}{\partial x_k}, \tag{14}$$

by using IMFM to specify V_l and post-processing $-\overline{u_i'v_j'}$ as described in Sec. II.

The desired rows of the averaged operator, $\overline{\mathcal{L}}$, in Eq. (11) are the same as the columns of its transpose, $\overline{\mathcal{L}}^{\top}$, which can be computed from Eq. (10) according to

$$\overline{\mathcal{L}}^{\top} = (E^{\top}\mathcal{L}^{-\top}P^{\top})^{-1} = (P\mathcal{L}^{-\top}E)^{-1}. \tag{15}$$

Equation (15) is similar to Eq. (10), and rather than inverting $\mathcal{L}^{\top}$ directly, IMFM can be used to compute columns of $\overline{\mathcal{L}}^{\top}$ by considering

$$\overline{\mathcal{L}}^{\top}V^{\dagger} = \overline{s^{\dagger}}, \tag{16}$$

which can be computationally assessed by forcing the following DNS equation:

$$\mathcal{L}^{\top}v^{\dagger} = s^{\dagger}, \tag{17}$$

where the dagger notation is used to distinguish Eqs. (16) and (17) from Eqs. (11) and (12). Here, Eq. (17) is a discretization of the adjoint of the GMT equations in Eqs. (3a) and (3b):

$$-\frac{\partial v_i^{\dagger}}{\partial t} - \frac{\partial u_j v_i^{\dagger}}{\partial x_j} = \frac{\partial q^{\dagger}}{\partial x_i} + \frac{1}{\text{Re}}\frac{\partial^2 v_i^{\dagger}}{\partial x_j \partial x_j} + s_i^{\dagger}, \tag{18a}$$

$$\frac{\partial v_i^{\dagger}}{\partial x_i} = 0, \tag{18b}$$

where $v_i^\dagger$ and $q^\dagger$ are the adjoint velocity and pressure, respectively. We define a reverse time $T \equiv t_f - t$, where t_f is the final simulation time, so

$$\frac{\partial v_i^\dagger}{\partial T} - \frac{\partial u_j v_i^\dagger}{\partial x_j} = \frac{\partial q^\dagger}{\partial x_i} + \frac{1}{\text{Re}}\frac{\partial^2 v_i^\dagger}{\partial x_j \partial x_j} + s_i^\dagger, \tag{19a}$$

$$\frac{\partial v_i^\dagger}{\partial x_i} = 0. \tag{19b}$$

The advective velocity fields, u_j, are first computed using a DNS of the incompressible Navier–Stokes equations in forward time order and then read in reverse time order for solving (19a). It is important to remark that the adjoint equations (19) are the dual of the GMT system and not the Navier–Stokes equations. As a result, these equations differ from the adjoint Navier–Stokes operator commonly adopted in nonlinear optimization and data assimilation [e.g., 21–23]. Specifically, the difference arises due to the treatment of the advection term, which is linear in the GMT system and is linearized when deriving the adjoint to the Navier–Stokes equations. In this regard, the adjoint GMT equation (19a) is therefore more akin to the adjoint to the scalar transport equation [24], but also additionally includes the adjoint pressure $q^\dagger$ and is accompanied by the divergence-free condition (19b).

As with the forward direction, rather than compute the columns of $\overline{\mathcal{L}}^\top$, we directly consider the transpose of the closure operator,

$$\overline{\mathcal{L}}^{\top\prime} = -\frac{\partial}{\partial x_i} D_{klij}^\top \frac{\partial}{\partial x_k}, \tag{20}$$

found by taking the transpose of $\overline{\mathcal{L}}'$ in Eq. (8). In considering the transpose of D_{ijkl}, the tensorial components are transposed such that $ijkl \to klij$, and the transpose notation $\top$ denotes swapping the rows and columns, e.g., $D(\mathbf{x}, \mathbf{y}) \to D(\mathbf{y}, \mathbf{x})$. The closure term for the adjoint equation in Eq. (19a) is

$$\overline{\mathcal{L}}^{\top\prime} V^\dagger = -\frac{\partial}{\partial x_i}\overline{u_i' v_j^{\dagger\prime}} = -\frac{\partial}{\partial x_i} D_{klij}^\top \frac{\partial V_l^\dagger}{\partial x_k}. \tag{21}$$

A column of $D_{klij}^\top$ can be obtained by using IMFM to specify the adjoint mean velocity gradient, solving the adjoint GMT equations in Eqs. (19a) and (19b), and post-processing the adjoint Reynolds stress.

For example, consider the discretization of the (nonadjoint) generalized eddy viscosity of Eq. (4):

$$\begin{bmatrix} -\overline{u_1' v_1'} \\ -\overline{u_1' v_2'} \\ -\overline{u_1' v_3'} \\ -\overline{u_2' v_1'} \\ \vdots \\ -\overline{u_3' v_3'} \end{bmatrix} = \begin{bmatrix} D_{1111} & D_{1112} & D_{1113} & D_{1121} & \dots & D_{1133} \\ D_{1211} & D_{1212} & D_{1213} & D_{1221} & \dots & D_{1233} \\ D_{1311} & D_{1312} & D_{1313} & D_{1321} & \dots & D_{1333} \\ D_{2111} & D_{2112} & D_{2113} & D_{2121} & \dots & D_{2133} \\ \vdots & \vdots & \vdots & \vdots & \ddots & \vdots \\ D_{3311} & D_{3312} & D_{3313} & D_{3321} & \dots & D_{3333} \end{bmatrix} \begin{bmatrix} \partial V_1/\partial x_1 \\ \partial V_2/\partial x_1 \\ \partial V_3/\partial x_1 \\ \partial V_1/\partial x_2 \\ \vdots \\ \partial V_3/\partial x_3 \end{bmatrix}, \tag{22}$$

where for each $i, j, k, l \in \{1, 2, 3\}$, $-\overline{u_i' v_j'}$ is a $N \times 1$ vector, D_{ijkl} is a $N \times N$ block matrix, $\partial V_l/\partial x_k$ is a $N \times 1$ vector, and N is the number of degrees of freedom in the averaged space. In IMFM, as used by Park and Mani [6], forcing one element of $\partial V_1/\partial x_2$ to be nonzero and post-processing

$-\overline{u'_i v'_j}$ leads to one column in each D_{ij21} matrix. For adjoint MFM:

$$
\begin{bmatrix}
\overline{u'_1 v_1^{\dagger\prime}} \\
\overline{u'_1 v_2^{\dagger\prime}} \\
\overline{u'_1 v_3^{\dagger\prime}} \\
\overline{u'_2 v_1^{\dagger\prime}} \\
\vdots \\
\overline{u'_3 v_3^{\dagger\prime}}
\end{bmatrix}
=
\begin{bmatrix}
D_{1111}^{\top} & D_{1211}^{\top} & D_{1311}^{\top} & D_{2111}^{\top} & \ldots & D_{3311}^{\top} \\
D_{1112}^{\top} & D_{1212}^{\top} & D_{1312}^{\top} & D_{2112}^{\top} & \ldots & D_{3312}^{\top} \\
D_{1113}^{\top} & D_{1213}^{\top} & D_{1313}^{\top} & D_{2113}^{\top} & \ldots & D_{3313}^{\top} \\
D_{1121}^{\top} & D_{1221}^{\top} & D_{1321}^{\top} & D_{2121}^{\top} & \ldots & D_{3321}^{\top} \\
\vdots & \vdots & \vdots & \vdots & \ddots & \vdots \\
D_{1133}^{\top} & D_{1233}^{\top} & D_{1333}^{\top} & D_{2133}^{\top} & \ldots & D_{3333}^{\top}
\end{bmatrix}
\begin{bmatrix}
\partial V_1^{\dagger}/\partial x_1 \\
\partial V_2^{\dagger}/\partial x_1 \\
\partial V_3^{\dagger}/\partial x_1 \\
\partial V_1^{\dagger}/\partial x_2 \\
\vdots \\
\partial V_3^{\dagger}/\partial x_3
\end{bmatrix}. \tag{23}
$$

Forcing one element of $\partial V_1^{\dagger}/\partial x_2$ to be nonzero and post-processing $\overline{u'_i v_j^{\dagger\prime}}$ leads to one column in each $D_{21ij}^{\top}$ matrix, i.e., a row in each D_{21ij} matrix. If, for example, a row of D_{1121} is desired instead, then one should force an element of $\partial V_1^{\dagger}/\partial x_1$ and post-process $\overline{u'_2 v_1^{\dagger\prime}}$ in a separate simulation. The general expression in continuous form is

$$
\overline{u'_k v_l^{\dagger\prime}}(\mathbf{y}, \tau) = \int_{\mathbf{x},t} D_{ijkl}(\mathbf{x}, \mathbf{y}, t, \tau) \frac{\partial V_j^{\dagger}}{\partial x_i}\bigg|_{\mathbf{x},t} d\mathbf{x} dt, \tag{24}
$$

where we have relabeled the indices $i \leftrightarrow k$ and $j \leftrightarrow l$ and the coordinates $\mathbf{x} \leftrightarrow \mathbf{y}$ and $t \leftrightarrow \tau$ to keep the ordering in $D_{ijkl}(\mathbf{x}, \mathbf{y}, t, \tau)$ identical to the eddy viscosity kernel in Eq. (4).

Adjoint MFM for passive scalar transport is shown in Appendix B. As a simpler case than momentum transport, the derivation for passive scalar transport more clearly shows the transposition of the indices to arrive at Eq. (20).

IV. CHANNEL SETUP AND NUMERICAL DETAILS

For the turbulent channel flow DNS, we use the three-dimensional incompressible Navier–Stokes solver developed by Bose *et al.* [25] and modified by Seo *et al.* [26]. The flow is driven by a nondimensionalized mean pressure gradient, $r_i = (1, 0, 0)$. The Reynolds number, $\mathrm{Re}_\tau = u_\tau \delta/\nu$, is defined based on the channel half-height, $\delta = 1$, and friction velocity, $u_\tau = 1$.

Park and Mani [6] modified the solver to include the GMT equations in Eqs. (3a) and (3b). We modified the solver for the adjoint GMT equations in Eqs. (19a) and (19b). We first conduct a DNS with output fields u_j at each timestep. We then solve Eq. (19a) by stepping backward in time and reading the u_j fields in reverse order. The solenoidal condition in Eq. (19b) is enforced using a fractional-step method. The post-processing involves averaged statistics, not instantaneous flow fields, so the differences between continuous and discrete adjoint formulations are unimportant [27].

Periodic boundary conditions are enforced in the streamwise (x_1) and spanwise (x_3) directions, and no-slip and no-penetration boundary conditions are enforced at the walls. All solvers use semi-implicit time advancement [28]; second-order Crank–Nicolson is used for the wall-normal diffusion terms, and Adams–Bashforth is used for all other terms. For spatial discretization, the solvers use second-order finite differences on a staggered mesh [29] with uniform spacing in x_1 and x_3 and nonuniform spacing in x_2. The pressure Poisson equation is solved using Fourier transforms in the periodic x_1 and x_3 directions and a tridiagonal solver in the x_2 direction.

For the 1D wall-normal eddy viscosity, Park and Mani [6] used a domain size of $L_1 \times L_2 \times L_3 = 2\pi \times 2 \times \pi$ with $N = 144$ grid cells in each direction, which we follow for comparison purposes. For the 2D streamwise and wall-normal eddy viscosity, due to the long streamwise extent of the eddy viscosity kernel, we doubled the domain size in the x_1 direction to $L_1 = 4\pi$. The resolution and remaining directions are unchanged from Park and Mani [6].

A. Obtaining rows of D_{2121} for the 1D wall-normal eddy viscosity

For the 1D wall-normal eddy viscosity, Park and Mani [6] specified the mean streamwise velocity as Heaviside functions, $V_1 = \theta(x_2 - x_2^*)$, at wall-normal locations, x_2^*, which are maintained by the forcing. This specifies the mean velocity gradient as a Dirac δ function, $\partial V_1 / \partial x_2 = \delta(x_2 - x_2^*)$. Park and Mani [6] then post-processed $-\overline{u_2' v_1'}$ to obtain the column of D_{2121} at x_2^* and repeated the procedure for all x_2^*. The adjoint mean streamwise velocity is also specified as a Heaviside function, and post-processing of $\overline{u_2' v_1^{\dagger'}}$ leads to a row of D_{2121}.

B. Obtaining rows of other components of D_{ij21} for the 1D wall-normal eddy viscosity

For other components, which require maintaining adjoint mean velocity gradient directions other than $\partial V_1^\dagger / \partial x_2$ as Dirac δ functions, specifying the adjoint mean velocity fields as Heaviside functions may not be mathematically well-posed. For example, obtaining a row of D_{1121} requires specifying $\partial V_1^\dagger / \partial x_1$ as a Dirac δ function, $\partial V_1^\dagger / \partial x_1 = \delta(x_2 - x_2^*)$, and post-processing $\overline{u_2' v_1^{\dagger'}}$. An adjoint mean velocity field that satisfies both $\partial V_1^\dagger / \partial x_1 = \delta(x_2 - x_2^*)$ and $\partial V_1^\dagger / \partial x_2 = 0$ does not exist. Thus, we decompose the adjoint velocity field into $v_i^\dagger = V_i^\dagger + v_i^{\dagger'}$, specify $\partial V_1^\dagger / \partial x_1$ analytically, and solve the corresponding equation for $v_i^{\dagger'}$. In other words, the decomposition is substituted into the adjoint GMT equation in Eq. (19a):

$$\frac{\partial V_i^\dagger}{\partial T} + \frac{\partial v_i^{\dagger'}}{\partial T} - u_j \frac{\partial V_i^\dagger}{\partial x_j} - u_j \frac{\partial v_i^{\dagger'}}{\partial x_j} = \frac{\partial q^\dagger}{\partial x_i} + \frac{1}{\mathrm{Re}} \frac{\partial^2 V_i^\dagger}{\partial x_j \partial x_j} + \frac{1}{\mathrm{Re}} \frac{\partial^2 v_i^{\dagger'}}{\partial x_j \partial x_j} + s_i^\dagger, \tag{25}$$

and $\partial V_i^\dagger / \partial x_j$ is analytically specified. The IMFM forcing, $s_i^\dagger$, now maintains $\overline{v_i^{\dagger'}} = 0$. For further simplification, the mean temporal term and mean diffusion term may be absorbed by the forcing since they adhere to the property $s_i^\dagger = \overline{s_i^\dagger}$:

$$\frac{\partial v_i^{\dagger'}}{\partial T} - u_j \frac{\partial V_i^\dagger}{\partial x_j} - u_j \frac{\partial v_i^{\dagger'}}{\partial x_j} = \frac{\partial q^\dagger}{\partial x_i} + \frac{1}{\mathrm{Re}} \frac{\partial^2 v_i^{\dagger'}}{\partial x_j \partial x_j} + s_i^\dagger. \tag{26}$$

Continuing the above example for obtaining a row of D_{1121}, substituting $\partial V_1^\dagger / \partial x_1 = \delta(x_2 - x_2^*)$ into (26) leads to the following equation for $v_i^{\dagger'}$:

$$\frac{\partial v_i^{\dagger'}}{\partial T} - u_1 \delta(x_2 - x_2^*) \delta_{i1} - \frac{\partial u_j v_i^{\dagger'}}{\partial x_j} = \frac{\partial q^\dagger}{\partial x_i} + \frac{1}{\mathrm{Re}} \frac{\partial^2 v_i^{\dagger'}}{\partial x_j \partial x_j} + s_i^\dagger, \tag{27}$$

where δ_{i1} is the Kronecker δ and $s_i^\dagger$ maintains $\overline{v_i^{\dagger'}} = 0$. We enforce a solenoidal $v_i^{\dagger'}$ as

$$\frac{\partial v_i^{\dagger'}}{\partial x_i} = 0. \tag{28}$$

While the solenoidal condition is enforced on $v_i^{\dagger'}$, the analytically specified adjoint mean velocity gradient may not be solenoidal, e.g., when $\partial V_1^\dagger / \partial x_1 = \delta(x_2 - x_2^*)$ and all other adjoint mean velocity gradient components are zero. Because the GMT equations in Eqs. (3a) and (3b) are linear and ultimately only the superposition of the components of D_{ijkl} is needed for the Reynolds stress tensor, we relax the solenoidal constraint on the adjoint mean velocity gradient to ease computation of the individual components of D_{ijkl} by activating various components of the adjoint mean velocity gradient independently. Alternatively, the adjoint mean velocity gradient can be considered an IMFM forcing to the governing equation for $v_i^\dagger$ that satisfies the requisite property $s^\dagger = \overline{s^\dagger}$.

C. Obtaining rows of D_{ijkl} for the 2D streamwise and wall-normal eddy viscosity

The 2D streamwise and wall-normal eddy viscosity for statistically stationary turbulent channel flow is:

$$-\overline{u_i' u_j'}(x_1, x_2) = \int_{y_1, y_2} D_{ij21}(x_1, x_2, y_1, y_2) \frac{\partial U_1}{\partial x_2}\bigg|_{y_1, y_2} dy_1 dy_2, \tag{29}$$

where averaging is taken in time and the homogeneous spanwise (x_3) direction. Using adjoint MFM:

$$\overline{u_k' v_l^{\dagger'}}(y_1, y_2) = \int_{x_1, x_2} D_{ijkl}(x_1, x_2, y_1, y_2) \frac{\partial V_j^{\dagger}}{\partial x_i}\bigg|_{x_1, x_2} dx_1 dx_2. \tag{30}$$

For example, the nonlocal eddy viscosity component, D_{2121}, corresponding to the influence of the mean velocity gradient, $\partial V_1/\partial x_2$, on the shear component of the Reynolds stress, $-\overline{u_2' v_1'}$, using adjoint MFM is

$$\overline{u_2' v_1^{\dagger'}}(y_1, y_2) = \int_{x_1, x_2} D_{2121}(x_1, x_2, y_1, y_2) \frac{\partial V_1^{\dagger}}{\partial x_2}\bigg|_{x_1, x_2} dx_1 dx_2, \tag{31}$$

where we specify $\partial V_1^{\dagger}/\partial x_2 = \delta(x_1 - x_1^*)\delta(x_2 - x_2^*)$ and zero for all other adjoint mean velocity gradient components, and post-process $\overline{u_2' v_1^{\dagger'}}(y_1, y_2)$ to obtain $D_{2121}(x_1 = x_1^*, x_2 = x_2^*, y_1, y_2)$. The flow is homogeneous in the x_1 direction, so x_1^* can be *any* streamwise location, and the eddy viscosity is a function of the distance, $y_1 - x_1$. Instead of reporting the 2D eddy viscosity kernel as $D_{ijkl}(x_1, x_2, y_1, y_2)$, we will omit the first input and report $D_{ijkl}(x_2, y_1 - x_1, y_2)$.

Similar to Sec. IV B, specifying the adjoint mean velocity field as a Heaviside function to enforce the mean velocity gradient as a Dirac δ function is not mathematically well-posed. For example, an adjoint mean velocity field that satisfies $\partial V_1^{\dagger}/\partial x_2 = \delta(x_1 - x_1^*)\delta(x_2 - x_2^*)$ and $\partial V_1^{\dagger}/\partial x_1 = 0$ does not exist. Thus, similar to Sec. IV B, we decompose the adjoint velocity field into $v_i^{\dagger} = V_i^{\dagger} + v_i^{\dagger'}$ and specify $\partial V_1^{\dagger}/\partial x_2$ analytically in the equation for $v_i^{\dagger'}$. The decomposition allows us to examine each component of D_{ijkl} independently and does not violate any mathematical constraints when a consistent superposition of the various components of the mean velocity gradient appears in the RANS equation. Computing other components of the nonlocal eddy viscosity is similar to Sec. IV B, where adjoint MFM transposes the components of D_{ijkl}.

V. RESULTS

A. One-dimensional wall-normal eddy viscosity comparison

For verification, we compare the 1D wall-normal eddy viscosity at one location, $x_2 = -0.565$, obtained using the adjoint formulation with that of Park and Mani [6] obtained using a brute-force approach at $\mathrm{Re}_\tau = 180$. We chose $x_2 = -0.565$, corresponding to row 50 out of 144, due to its significant asymmetry in the row versus column as shown in Fig. 3, although we expect the results to hold for all x_2 locations. Park and Mani [6] averaged over 500 eddy turnover time (δ/u_τ) for their modeling purposes, whereas we averaged over 115 eddy turnover time, which we found sufficient for verification purposes.

Figure 4 shows the eddy viscosity from the adjoint formulation closely matching that of Park and Mani [6]. The normalized error is less than 1%. We attribute this error to statistical convergence and the shorter averaging times used. For example, the normalized error of a regular MFM calculation averaged over 115 eddy turnover time and compared with the corresponding column is 0.7%, and the normalized error of the adjoint MFM calculation used here is 0.8%. Therefore, the differences in Fig. 4 are within the uncertainty bounds of the calculation.

Figure 5 shows a comparison for the other components of D_{ij21}, which are even more asymmetric with regards to rows versus columns as shown in Appendix C. Note D_{2121} in Fig. 4 is not expected
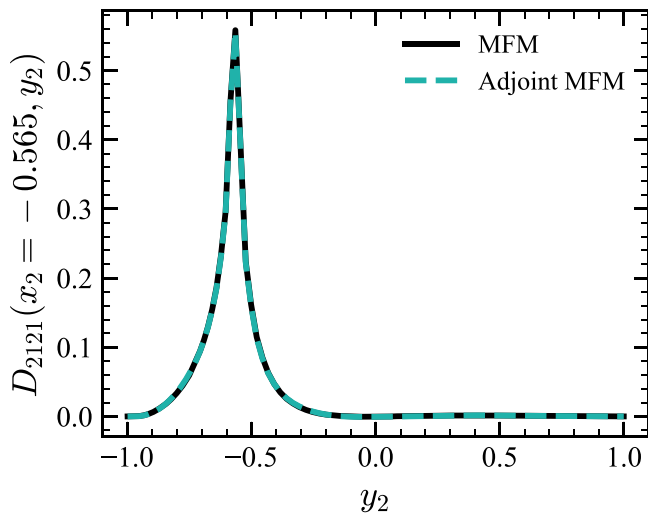
FIG. 4. Comparison of $D_{2121}(x_2 = -0.565, y_2)$ using adjoint MFM and from a brute-force calculation by Ref. [6] using MFM.
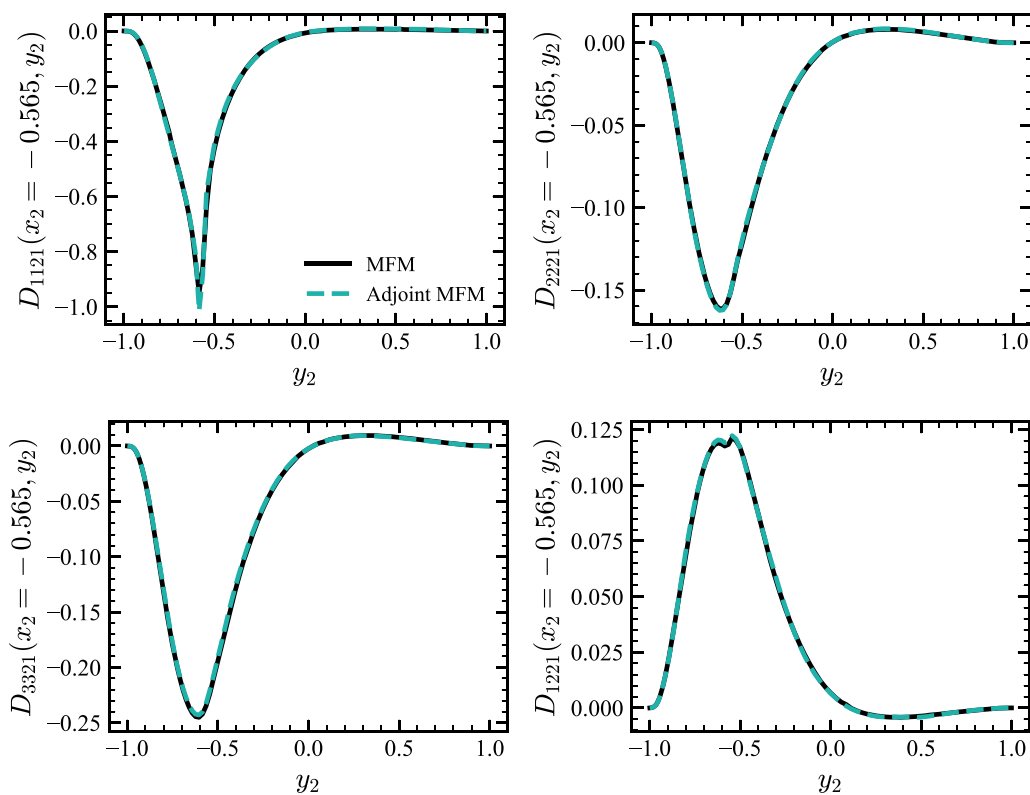

FIG. 5. Comparison of other components of $D_{ij21}(x_2 = -0.565, y_2)$ using adjoint MFM and from a brute-force calculation by Ref. [6] using MFM.

to be identical to D_{1212} in Fig. 5 because $\overline{u_2' v_1'}$ and $\overline{u_1' v_2'}$ have different meanings. We first focused on $\overline{u_2' v_1'}$ because it is the term that appears in the RANS equation for the streamwise mean velocity and corresponds to the mixing of the streamwise momentum fluctuations v_1' by the wall-normal fluctuations u_2'. Conversely, $\overline{u_1' v_2'}$ appears in the RANS equation for the wall-normal mean velocity and corresponds to the mixing of the wall-normal momentum fluctuations v_2'. Park and Mani [6] showed that the expected property $-\overline{u_2' u_1'} = \int D_{2121}(x_2, y_2) \partial U_1 / \partial x_2|_{y_2} \mathrm{d}y_2 = \int D_{1221}(x_2, y_2) \partial U_1 / \partial x_2|_{y_2} \mathrm{d}y_2$ is satisfied. Hamba [5] enforced symmetry in the eddy viscosity by averaging the two eddy viscosity components, e.g., $(D_{2121} + D_{1221})/2$, whereas Park and Mani [6] did not in light of the equality property mentioned above.

In Fig. 5, due to differences in enforcement of the mean velocity gradient as detailed in Sec. IV B and the staggered mesh, there is some error due to interpolation. However, the eddy viscosity from the adjoint formulation still closely matches that of Park and Mani [6]. The largest errors are in D_{1121} due to interpolating a sharp peak with 4% normalized error. The normalized error for all other cases is less than 1.5%.

A local approximation is valid if the width of the eddy viscosity kernel is much smaller than the lengthscale over which the mean velocity gradient varies. A local approximation would model the eddy viscosity as a Dirac δ function such that the Reynolds stress at a given location depends only on the mean velocity gradient at that same location. As an estimate of the kernel width of $D_{2121}(x_2 = -0.565, y_2)$ in Fig. 4, the eddy viscosity kernel drops to $1/3$ of its maximum value at $y_2 = -0.64$ and $y_2 = -0.51$. The mean velocity gradient changes from 7.4 to 5.6 in this region, which is a factor of 1.3. This change in the mean velocity gradient is nonnegligible, and we cannot conclude that the eddy viscosity is local. This is addressed in more detail in Park and Mani [6] and Hamba [5], which discuss the effect of a local eddy viscosity approximation on the Reynolds stresses and the mean velocity. Adjoint MFM enables efficient computation of the nonlocal eddy viscosity to analyze these effects for desired regions of the domain.

B. Cost comparison

A brute-force approach to obtaining the eddy viscosity requires as many simulations as degrees of freedom in the averaged space, which for the 1D wall-normal eddy viscosity considered in the previous section is $N = 144$. Each simulation solves both Navier–Stokes and GMT equations for a total of 288 DNSs. The proposed adjoint simulation uses one simulation per desired eddy viscosity location, which includes a forward solve of the Navier–Stokes equations and a backward solve of the GMT equations for a total of 2 DNSs. Additional overhead is associated with reading and writing the velocity fields to disk for the adjoint simulation, and more storage is needed. The storage requirements of adjoint MFM are identical to those for traditional adjoint solvers for turbulent flow problems, and for problems where storage may be an issue, checkpointing can be used [30,31].

For problems with many degrees of freedom in the averaged space, obtaining the eddy viscosity using a brute-force approach may be computationally cost-prohibitive. For example, extension to higher dimensions to examine the 2D streamwise and wall-normal nonlocal eddy viscosity would need 288×144 ($N_1 \times N_2$) simulations. However, using a single simulation, the adjoint-based formulation enables targeted quantification of the eddy viscosity at any desired location.

C. Two-dimensional streamwise and wall-normal eddy viscosity

We now use adjoint MFM to quantify the 2D streamwise and wall-normal eddy viscosity at near-wall locations in turbulent channel flow at $\mathrm{Re}_\tau = 180$. While the flow is homogeneous in the streamwise direction, we use turbulent channel flow to qualitatively gain a physical understanding of streamwise nonlocal effects in other wall-bounded flows, such as spatially developing boundary layers.

In Sec. V C 1, we show the 2D nonlocal eddy viscosity kernel for the shear component of the Reynolds stress at several near-wall locations. In Sec. V C 2, we compare the row and column of
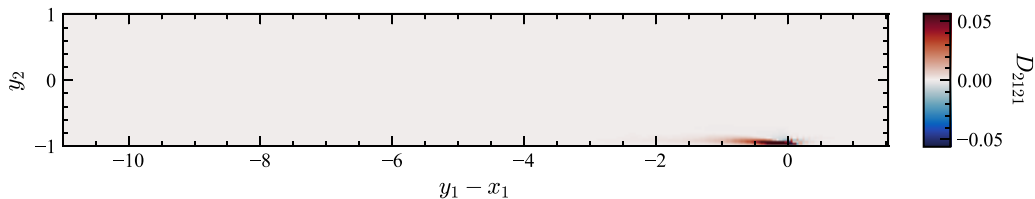
FIG. 6. Streamwise and wall-normal eddy viscosity kernel, $D_{2121}(x_2 = -0.946, y_1 - x_1, y_2)$, corresponding to the influence of the mean velocity gradient, $\partial V_1 / \partial x_2$, on the shear component of the Reynolds stress, $-\overline{u'_2 v'_1}$. The color bar is truncated at 10% of maximum absolute value to highlight better the region of upstream influence on the Reynolds stress.

the 2D eddy viscosity kernel. The row captures the dependence of the Reynolds stress at a given location on the mean velocity gradient upstream; the column captures the influence of the mean velocity gradient at a given location on the Reynolds stress downstream. We show that the rows and columns of the 2D nonlocal eddy viscosity are not identical, necessitating adjoint MFM to efficiently compute the more physically relevant rows. In Sec. V C 3, we quantify the streamwise nonlocality lengthscale based on the first-order streamwise moment of the eddy viscosity. In Sec. V C 4, we compare this with the estimate for the streamwise nonlocality lengthscale of Park *et al.* [32] formed by the first-order temporal moment of the eddy viscosity and the local mean velocity and discuss the modeling implications of differences in these lengthscales. Lastly, in Sec. V C 5, we examine the anisotropy in the 2D nonlocal eddy viscosity kernel by comparing other components of the mean velocity gradient tensor and Reynolds stress tensor.

1. D_{2121} component of the 2D eddy viscosity

Figure 6 shows the D_{2121} component of the 2D streamwise and wall-normal eddy viscosity, corresponding to the influence of the mean velocity gradient, $\partial V_1 / \partial x_2$, on the shear component of the Reynolds stress, $-\overline{u'_2 v'_1}$, at $x_2 = -0.946$. This location corresponds to $x_2^+ \approx 10$ when measured from the bottom wall in viscous units, i.e., $x_2^+ = (1 + x_2)/\delta_v$, which is in the buffer layer and near the location of maximum streamwise fluctuation and peak production, $x_2^+ \approx 12$ [33]. The color bar is truncated at 10% of the maximum absolute value to highlight better the region of upstream influence on the Reynolds stress. The results are averaged over 400 eddy turnover time (δ/u_τ).

Figure 6 shows oscillations near the forcing location due to the spatially singular nature of the forcing function. The thin region that needs to be resolved to avoid these oscillations is proportional to ν/U_1 where $\nu = 1/\mathrm{Re}_\tau = 1/180$ and $U_1 = 8.35$ at $x_2 = -0.946$. Resolving this region would require around 65 times finer mesh resolution than the current resolution, $\Delta x_1^+ = 7.85$. Appendix D shows the effect of mesh refinement and an upwind scheme rather than a central difference scheme.

To further establish confidence in the quantified eddy viscosity kernels, in Fig. 7, we show a comparison with the 1D wall-normal nonlocal eddy viscosity computed by Park and Mani [6]. For comparison purposes, the 2D kernel in Fig. 6 is integrated over the streamwise direction, resulting in an eddy viscosity that is local in the streamwise direction and nonlocal in the wall-normal direction, similar to Park and Mani [6]. The error in Fig. 7, hardly visible in the plot, is due to interpolation and differences in Dirac δ function location on a staggered mesh.

Figure 6 shows that the streamwise extent of the eddy viscosity kernel is much longer than the wall-normal extent. Qualitatively, this is expected due to the larger mean streamwise flow. With farther upstream distance from the peak (more negative $y_1 - x_1$), the kernel diminishes and spreads farther away from the wall. At the wall, the kernel diminishes to zero as expected due to diminishing transport from the wall-normal velocity fluctuations u'_2 and the wall boundary conditions.

Figure 8 shows the D_{2121} component of the 2D eddy viscosity kernel for several near-wall locations (from top to bottom): $x_2 = -0.978$ ($x_2^+ \approx 4$, viscous sublayer), $x_2 = -0.946$ ($x_2^+ \approx 10$, buffer layer), $x_2 = -0.859$ ($x_2^+ \approx 25$, buffer layer), $x_2 = -0.819$ ($x_2^+ \approx 33$, beginning of the log
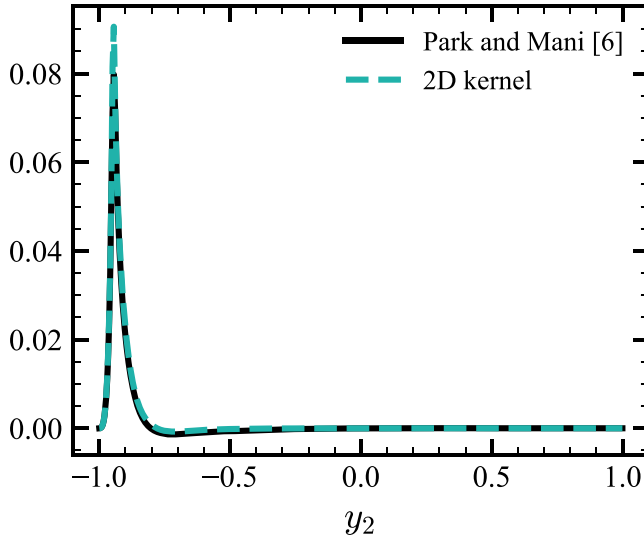
FIG. 7. Comparison of the 2D eddy viscosity kernel, $D_{2121}(x_2 = -0.946, y_1 - x_1, y_2)$, integrated over the streamwise direction and the 1D wall-normal eddy viscosity kernel of Park and Mani [6]. There is a small amount of error due to interpolation.

layer). The streamwise influence of the mean velocity gradient on the shear component of the Reynolds stress both grows in magnitude and length with increasing distance from the wall. In Sec. V C 3, we quantify this effect as a streamwise nonlocality lengthscale. The maximum of the color bar is truncated at ± 0.056, corresponding to 10% of the maximum absolute value of the 2D eddy viscosity kernel for $x_2 = -0.946$.

2. Comparison of streamwise row and streamwise column

We next compare $D_{2121}(x_2 = x_2^*, y_1 - x_1, y_2)$, e.g., as shown in Fig. 8, with $D_{2121}(x_2, y_1 - x_1, y_2 = x_2^*)$. As discussed in Sec. II for a 1D eddy viscosity that is nonlocal in the wall-normal direction, $D_{2121}(x_2 = x_2^*, y_1 - x_1, y_2)$ is a row of the discretized eddy viscosity matrix (now in a 2D sense) showing the dependence of the shear component of the Reynolds stress at x_2^* on the mean velocity gradient at all points in space. For comparison, $D_{2121}(x_2, y_1 - x_1, y_2 = x_2^*)$ is a column of the discretized eddy viscosity matrix showing the influence of the mean velocity gradient at x_2^* on the Reynolds stresses everywhere in the domain. Section II showed that for a 1D eddy viscosity that is nonlocal in the wall-normal direction, the rows and columns of the discretized eddy viscosity are not identical for turbulent channel flow, necessitating the use of adjoint MFM for efficiently computing rows of the eddy viscosity. This section investigates the 2D eddy viscosity and focuses on nonlocality in the streamwise direction.

Figures 9 and 10 show a comparison of $D_{2121}(x_2 = x_2^*, y_1 - x_1, y_2)$ and $D_{2121}(x_2, y_1 - x_1, y_2 = x_2^*)$ at $x_2^* = -0.946$ ($x_2^+ \approx 10$) and $x_2^* = -0.859$ ($x_2^+ \approx 25$), respectively. The column, $D_{2121}(x_2, y_1 - x_1, y_2 = x_2^*)$, is computed by using IMFM to specify $\partial V_1 / \partial x_2 = \delta(x_1 - x_1^*)\delta(x_2 - x_2^*)$ and zero for all other velocity gradient components and post-processing $-\overline{u_2' v_1'}$. The color bars are truncated in both figures at 10% of their respective maximum absolute values. $D_{2121}(x_2, y_1 - x_1, y_2 = x_2^*)$ (column) has a slightly longer streamwise nonlocality lengthscale than $D_{2121}(x_2 = x_2^*, y_1 - x_1, y_2)$ (row), which becomes more apparent for kernels that are farther away from the wall, e.g., at $x_2^+ \approx 25$ as shown in Fig. 10. This difference is seen more clearly in Fig. 11, which shows the kernels integrated over the wall-normal direction. Even though the flow is homogeneous
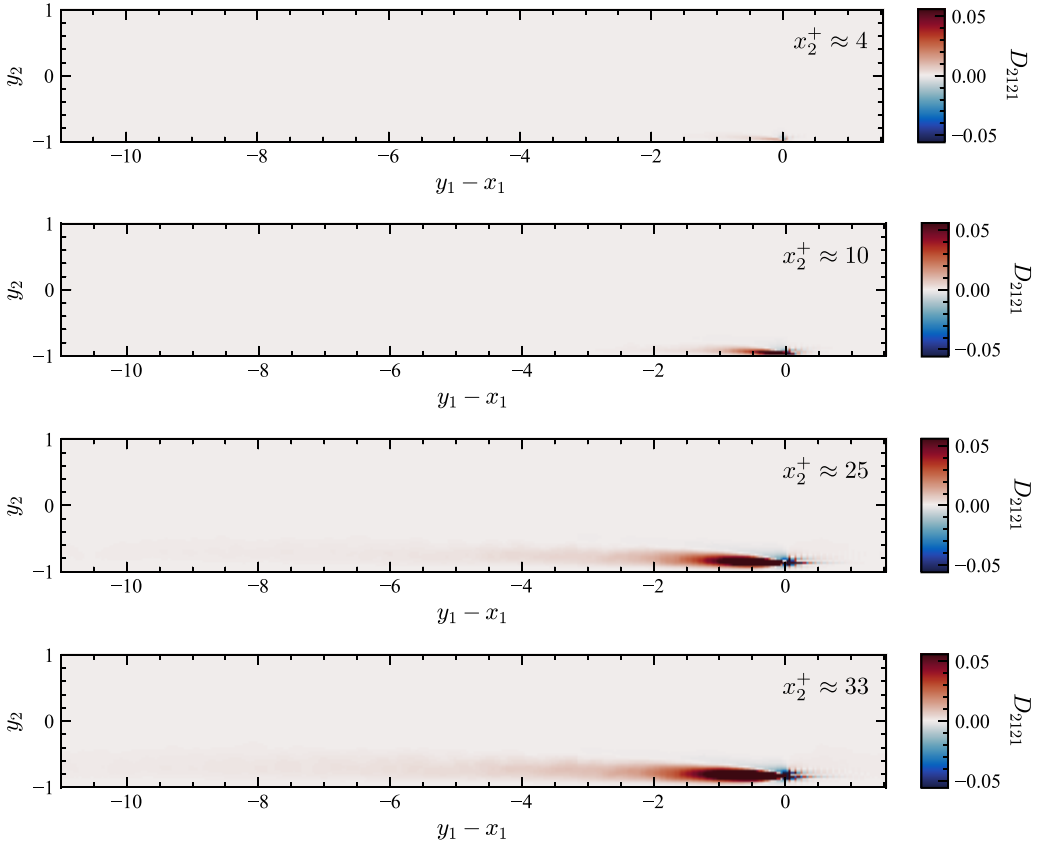
FIG. 8. $D_{2121}(x_2, y_1 - x_1, y_2)$ for several wall-normal locations (from top to bottom): $x_2 = -0.978$ ($x_2^+ \approx 4$, viscous sublayer), $x_2 = -0.946$ ($x_2^+ \approx 10$, buffer layer), $x_2 = -0.859$ ($x_2^+ \approx 25$, buffer layer), $x_2 = -0.819$ ($x_2^+ \approx 33$, beginning of the log layer).
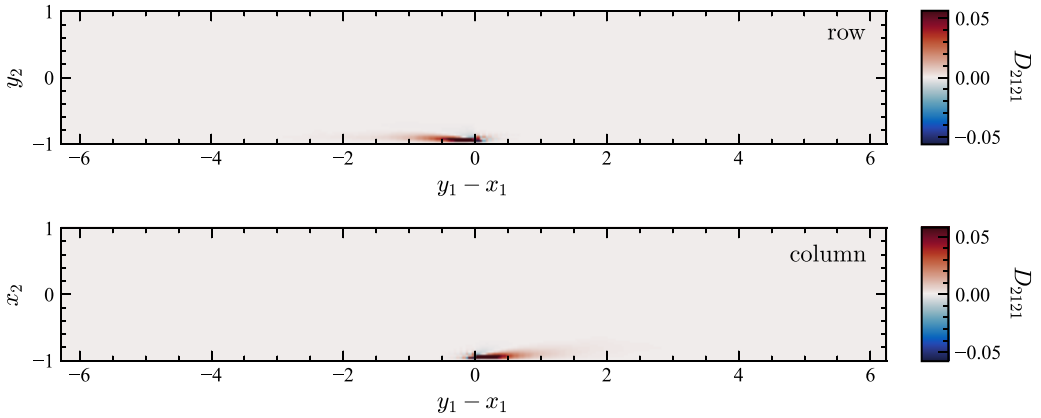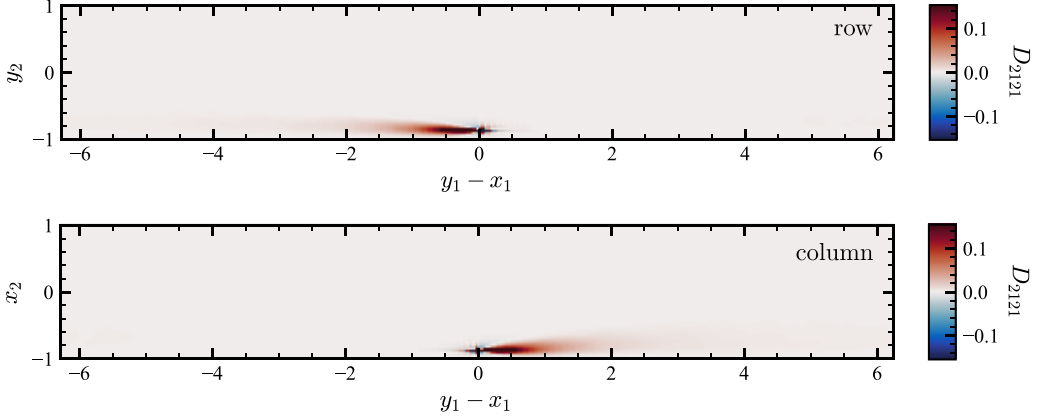

FIG. 9. Comparison of $D_{2121}(x_2 = -0.946, y_1 - x_1, y_2)$ (row) and $D_{2121}(x_2, y_1 - x_1, y_2 = -0.946)$ (column). The location $x_2^* = -0.946$ corresponds to $x_2^+ \approx 10$ (buffer layer).

FIG. 10. Comparison of $D_{2121}(x_2 = -0.859, y_1 - x_1, y_2)$ (row) and $D_{2121}(x_2, y_1 - x_1, y_2 = -0.859)$ (column). The location $x_2^* = -0.859$ corresponds to $x_2^+ \approx 25$ (buffer layer). The maximum values are similar, while $D_{2121}(x_2, y_1 - x_1, y_2 = -0.859)$ (column) shows a slightly longer streamwise nonlocality lengthscale than $D_{2121}(x_2 = -0.859, y_1 - x_1, y_2)$ (row).

in the x_1 direction, the streamwise row, found by integrating the 2D nonlocal eddy viscosity kernel in the wall-normal direction, is not simply the reverse of the streamwise column as shown in Fig. 11.

3. Characterization of the streamwise nonlocality lengthscale

We characterize the streamwise nonlocality lengthscale based on the first-order streamwise moment of the eddy viscosity defined by

$$D_{2121}^{1_s}(x_2) = \iint (y_1 - x_1) D_{2121}(x_2, y_1 - x_1, y_2) dy_1 dy_2. \tag{32}$$
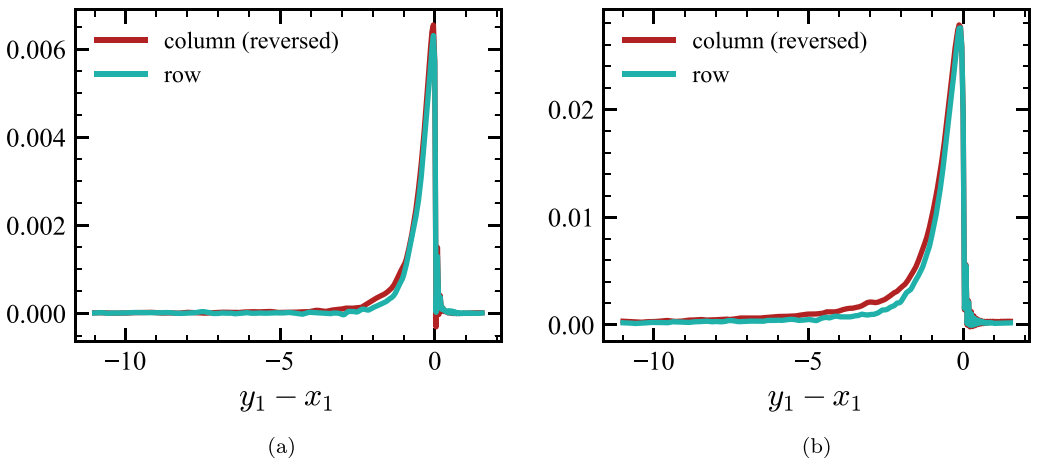
FIG. 11. (a) Comparison of the streamwise row at $x_2 = -0.946$ and streamwise column at $y_2 = -0.946$, and (b) comparison of the streamwise row at $x_2 = -0.859$ and streamwise column at $y_2 = -0.859$, computed by integrating the 2D kernels in Figs. 9 and 10, respectively, over the wall-normal direction. The streamwise column is reversed for comparison purposes to highlight that it is not identical to the streamwise row.
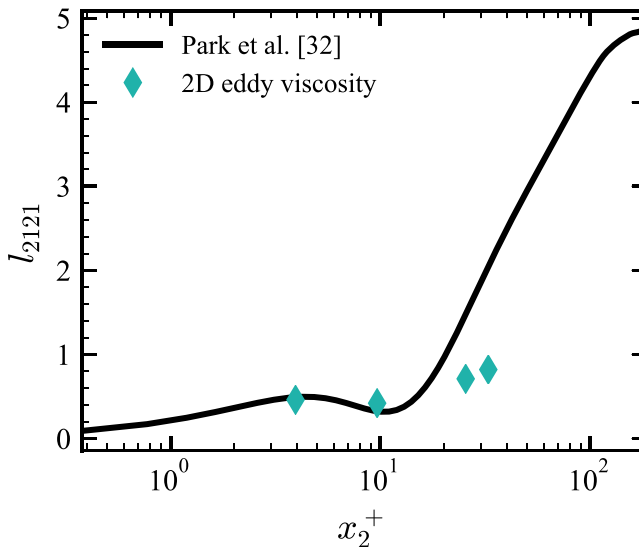
FIG. 12. Comparison between the streamwise nonlocality lengthscale estimated by Park *et al.* [32] using $T_{2121}U_1$, where $T_{2121} = -D^{1_t}_{2121}/D^0_{2121}$ and $D^{1_t}_{2121}$ is the first-order temporal moment, and the lengthscale calculated using $l_{2121} = -D^{1_s}_{2121}/D^0_{2121}$ from the 2D nonlocal eddy viscosity at $\mathrm{Re}_\tau = 180$.

The first-order streamwise moment characterizes the centroid of the eddy viscosity in the streamwise direction, given by a streamwise nonlocality lengthscale, $l_{2121} = -D^{1_s}_{2121}/D^0_{2121}$, where D^0_{2121} is the zeroth-order moment of the eddy viscosity:

$$D^0_{2121}(x_2) = \iint D_{2121}(x_2, y_1 - x_1, y_2) dy_1 dy_2. \tag{33}$$

Due to the periodicity in the x_1 direction, small but nonzero values of the eddy viscosity kernel away from the peak are heavily weighted by the distance from the peak in the calculation of $D^{1_s}_{2121}$. Hence, careful treatment of the integral in Eq. (32) is needed as detailed in Appendix E. The streamwise nonlocality lengthscale, l_{2121}, is computed for various wall-normal locations in Fig. 12.

4. Assessment of spatial nonlocality as a history effect in a Lagrangian framework

One way to interpret the long streamwise extent of the 2D nonlocal eddy viscosity kernel and the corresponding l_{2121} is by considering a temporal history effect along the trajectory of a fluid parcel that moves with the mean flow. This history effect can be characterized by an eddy viscosity kernel that is nonlocal in time and a corresponding temporal nonlocality timescale, $T_{2121} = -D^{1_t}_{2121}/D^0_{2121}$, where $D^{1_t}_{2121}$ is the first-order temporal moment. In Park *et al.* [32], we used MFM to directly compute $D^{1_t}_{2121}$. Because the velocity is constant along mean streamlines for turbulent channel flow, in a Lagrangian framework, the streamwise nonlocality lengthscale is related to the temporal nonlocality lengthscale via $T_{2121}U_1$, where U_1 is the local mean streamwise velocity. Figure 12 shows a comparison between the streamwise nonlocality length calculated using the 2D nonlocal eddy viscosity and the Lagrangian estimate based off of $T_{2121}U_1$ from Park *et al.* [32] at $\mathrm{Re}_\tau = 180$. As seen in Fig. 12, the two lengthscales are correlated, which is expected given the vivid upstream structure of the eddy viscosity kernel. These lengthscales may be used interchangeably for qualitative estimates of the magnitude of spatial or temporal nonlocality scales. However, as seen in Fig. 12, $l_{2121} = -D^{1_s}_{2121}/D^0_{2121}$ and $T_{2121}U_1$ are not identical, particularly starting in the buffer layer and into the log layer.
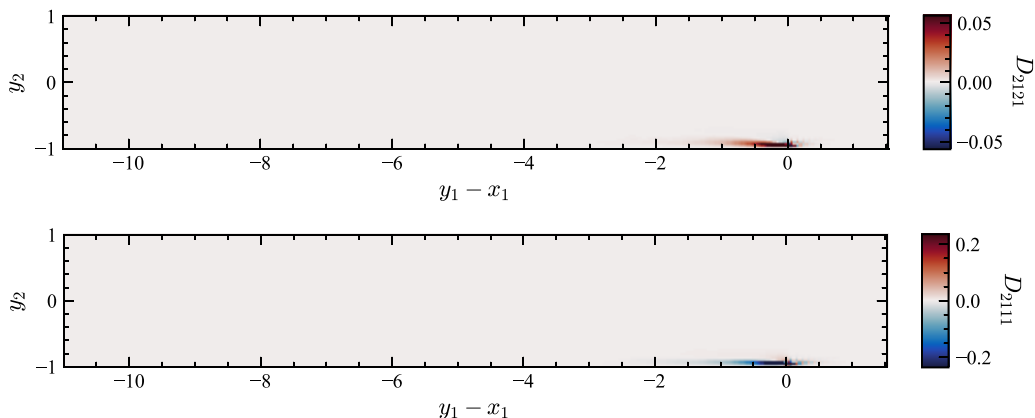
FIG. 13. Comparison between D_{2121} and D_{2111} at $x_2 = -0.946$ ($x_2^+ \approx 10$). The D_{2111} component shows the influence of streamwise gradient of the mean velocity, $\partial V_1/\partial x_1$, on the shear component of the Reynolds stress, $-\overline{u_2' v_1'}$.

This difference between l_{2121} and $T_{2121}U_1$ has implications for modeling and suggests modifications to the model form starting in the buffer layer. Models often include nonlocal effects by considering a history effect along Lagrangian trajectories using the material derivative and a relaxation timescale, e.g., Reynolds stress transport models [34,35]:

$$T \frac{D}{Dt} \overline{u_i' u_j'} = -\overline{u_i' u_j'} + \dots . \tag{34}$$

This formulation includes an implied streamwise nonlocality lengthscale TU_1 from the advection term. To match the measured streamwise nonlocality length, there should be additional terms with the first-order spatial derivative of the Reynolds stresses, e.g., $a \frac{\partial}{\partial x_1} \overline{u_i' u_j'}$. For example, this could be achieved with a cross-diffusion term or a spatially varying turbulent viscosity.

5. Assessment of anisotropy in the 2D eddy viscosity

In this section, we examine the anisotropy of the 2D eddy viscosity by considering other components of D_{ijkl}. We begin by examining the D_{21kl} components of eddy viscosity corresponding to the shear component of the Reynolds stress, $-\overline{u_2' v_1'}$, and other components of the mean velocity gradient tensor, $\partial V_l/\partial x_k$, specifically focusing on $\partial V_1/\partial x_1$. We then examine the D_{ij21} components of the eddy viscosity corresponding to the normal components of the Reynolds stress, $-\overline{u_i' v_j'}$, and the wall-normal mean velocity gradient, $\partial V_1/\partial x_2$.

Figure 13 shows a comparison of the D_{2121} and D_{2111} component of the eddy viscosity at $x_2 = -0.946$ ($x_2^+ \approx 10$). The D_{2111} component shows the influence of the streamwise gradient of the mean velocity, $\partial V_1/\partial x_1$, on the shear component of the Reynolds stress, $-\overline{u_2' v_1'}$. While $\partial V_1/\partial x_1$ is inactive in channel flow since x_1 is a homogeneous direction, this component would be active in a spatially developing boundary layer or a separated flow. We use the 2D eddy viscosity kernel from channel flow to qualitatively estimate the nonlocal effects present in other wall-bounded flows. Figure 13 shows that the D_{2111} component has a much larger magnitude than the D_{2121} component (the color bars are truncated at 10% of their maximum respective values), indicating that the shear component of the Reynolds stress has a greater sensitivity to $\partial V_1/\partial x_1$ than $\partial V_1/\partial x_2$. Figure 14 shows a similar comparison of the same two components for $x_2 = -0.859$ ($x_2^+ \approx 25$).

The $\overline{u_2' v_1'}$ component of the Reynolds stress tensor describes mixing of the streamwise momentum fluctuations, v_1', by wall-normal fluctuations, u_2'. The Boussinesq approximation would imply this mixing flux is sensitive only to the wall-normal gradient of the mean streamwise velocity.
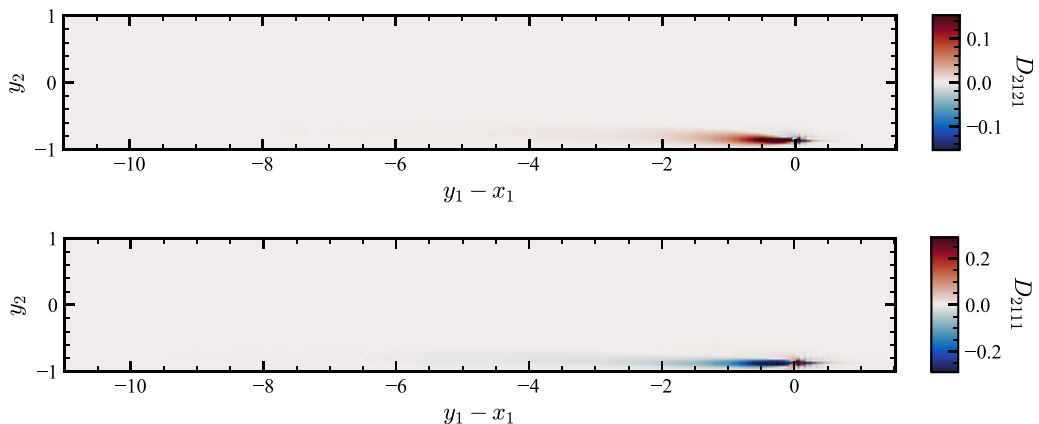
FIG. 14. Comparison between D_{2121} and D_{2111} at $x_2 = -0.859$ ($x_2^+ \approx 25$).

However, we observe a stronger sensitivity to the streamwise gradient (not only is it nonnegligible, but larger than the sensitivity to the wall-normal gradient).

We additionally examine anisotropy in the eddy viscosity by considering the influence of the wall-normal mean velocity gradient, $\partial V_1/\partial x_2$, on the normal components of the Reynolds stress tensor. Figure 15 shows a comparison between the shear component, D_{2121}, and normal components, D_{1121}, D_{2221}, D_{3321}, of the 2D nonlocal eddy viscosity kernel at $x_2 = -0.946$ ($x_2^+ \approx 10$). Each component is normalized by its respective zeroth-order moment, D_{ij21}^0. The color bar is truncated for easier visual comparison between the components. Due to the long extent of the streamwise nonlocality, the periodic domain affects D_{3321}. Appendix F discusses the domain effects on the eddy viscosity in more detail. The shear component D_{2121} has the shortest streamwise nonlocal effect, while the normal components have a much longer streamwise nonlocal effect.

Models that use an isotropic eddy viscosity, e.g., Spalart–Allmaras [2], Menter SST [3], and Wilcox k–ω [4] models, are unable to capture these effects. For example, under a local and isotropic approximation, $-\overline{u_i' u_j'} = 2\nu_T S_{ij}$, where ν_T is the eddy viscosity, and S_{ij} is the mean strain rate tensor. These models partially include history effects, i.e., dependence on the upstream conditions through a Lagrangian material derivative, by using evolution equations for the eddy viscosity (or equations for characteristic quantities that can be used to form the eddy viscosity, such as the turbulent kinetic energy scale k and dissipation scale ε). However, isotropic models use the same eddy viscosity for all components of the Reynolds stress. Figure 15 clearly shows differences in the upstream extent and magnitude of the eddy viscosity among different components of the Reynolds stresses. This anisotropy in the eddy viscosity for near-wall Reynolds stresses influences important aspects of wall-bounded flows, such as the prediction of the friction coefficient and separation.

Reynolds stress transport models [34,35] can capture anisotropy by using a transport equation for each component of the Reynolds stress. Most models use an isotropic history timescale, e.g., $T = k/\varepsilon$ for all components of the Reynolds stress tensor where k is the characteristic turbulent kinetic energy scale and ε is the characteristic dissipation scale. Model terms that couple the Reynolds stresses, e.g., the return to isotropy term, can modify the effective history timescale and thus the upstream dependence. The presented nonlocal kernel data in Fig. 15 provides a quantitative guide for the expected history timescales for Reynolds stress transport modeling.

VI. CONCLUSION

The generalized eddy viscosity at a specific location relates the Reynolds stress at that location to mean velocity gradients at all locations, which can be used to characterize nonlocality and
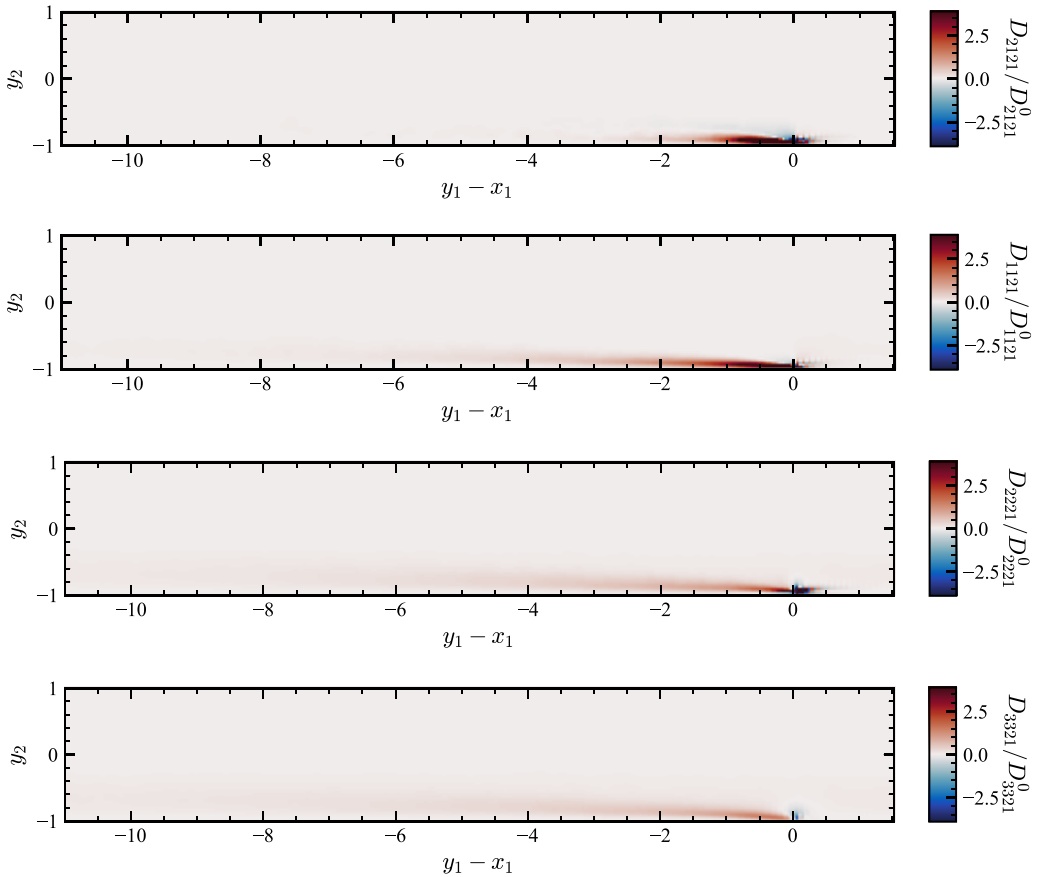
FIG. 15. Comparison between the shear component, D_{2121}, and the normal components, D_{1121}, D_{2221}, D_{3321}, of the 2D nonlocal eddy viscosity at $x_2 = -0.946$ ($x_2^+ \approx 10$). Each component is normalized by its respective zeroth-order moment, D_{ij21}^0.

sensitivity to the mean velocity gradient. In this work, we developed an adjoint-based MFM to cost-effectively compute the eddy viscosity at a specific location of the Reynolds stress using one simulation. Previous brute-force approaches [5,8] forced the mean velocity gradient at each location in the averaged space and computed the Reynolds stress response, requiring a separate simulation for each mean velocity gradient location. Hence, these approaches needed as many simulations as degrees of freedom in the averaged space.

Adjoint MFM can be used to compute the eddy viscosity in regions of interest in turbulent flows, such as at flow separation or reattachment points, to examine nonlocal effects and inform RANS models of deficiencies in their eddy viscosity approximations. A brute-force approach would characterize the eddy viscosity for the entire domain (including regions where RANS models perform adequately) and require many simulations. Conversely, adjoint MFM can be used for a more targeted computation of the eddy viscosity in only regions of interest and fewer simulations.

For applications where the generalized eddy viscosity for the entire domain is still desired, adjoint MFM can also aid in substantially reducing the number of simulations to approximate the discretized eddy viscosity operator. Fast MFM [16] leverages hidden sparsity in the discretized eddy viscosity and uses a limited number of forward and adjoint MFM simulations, such that each simulation contains information about multiple rows and columns. For example, for

the 1D wall-normal eddy viscosity of Park and Mani [6], which required $N = 144$ simulations using a brute-force approach, fast MFM uses $N = 20$ simulations to approximate the nonlocal eddy viscosity such that the reconstructed Reynolds stresses are virtually indistinguishable from DNS.

We then used adjoint MFM to investigate the streamwise and wall-normal extent of the eddy viscosity kernel in turbulent channel flow at several near-wall locations from the viscous sublayer to the log layer. The data files for the 2D kernels shown in Figs. 8, 9, 10, 13, 14, and 15 are available in the Supplemental Material [36]. While Park and Mani [6] and Hamba [5] showed that the rows and columns of the 1D wall-normal eddy viscosity are not identical in turbulent channel flow, we also found that the streamwise row (computed by integrating the 2D eddy viscosity kernel over the wall-normal direction) is not identical to the reverse of the streamwise column. The nonlocal influence of the streamwise column is slightly longer than that of the streamwise row and increases with distance from the wall. Physically, this implies that the mean velocity gradient at a given point influences the Reynolds stress farther downstream than the Reynolds stress at the same point is influenced by the mean velocity gradient upstream.

We also found the nonlocal eddy viscosity kernel is much longer in the streamwise direction than the wall-normal direction, and the nonlocality length in the streamwise direction increases with distance from the wall. This result is qualitatively expected due to the increase in the mean streamwise velocity with distance from the wall; however, we quantified this effect in this work. We then characterized the streamwise nonlocality lengthscale using $l_{2121} = -D_{2121}^{1_s}/D_{2121}^0$, where $D_{2121}^{1_s}$ is the first-order streamwise moment of the eddy viscosity and D_{2121}^0 is the zeroth-order moment of the eddy viscosity.

For comparison, we also considered a streamwise nonlocality lengthscale based on a history effect along Lagrangian trajectories, $T_{2121}U_1$, where $T_{2121} = -D_{2121}^{1_t}/D_{2121}^0$ and $D_{2121}^{1_t}$ is the first-order temporal moment. While l_{2121} and $T_{2121}U_1$ are correlated, we observed differences, particularly starting in the buffer layer and into the log layer. For modeling, this difference suggests modification of the streamwise nonlocality lengthscale associated with the material derivative, e.g., by including terms of the form $a\frac{\partial}{\partial x_1}\overline{u_i'u_j'}$, which may be cross-diffusion terms or a turbulent diffusion term with spatially varying viscosity.

We then examined the anisotropy of the 2D eddy viscosity kernel. We observed that while their streamwise extents are similar, D_{2111} has a larger magnitude than D_{2121}, i.e., the shear component of the Reynolds stress, $\overline{u_2'v_1'}$, is more sensitive to the streamwise gradient of the mean velocity, $\partial V_1/\partial x_1$, than the wall-normal gradient of the mean velocity, $\partial V_1/\partial x_2$. We also examined the anisotropy in the eddy viscosity kernels by comparing the normal components of the Reynolds stresses with the shear component. We found the eddy viscosity kernels have a longer streamwise extent for the normal components than the shear component.

These observations can be used to inform models of the needed anisotropy. While the Boussinesq approximation is qualitatively expected to be invalid, we quantified the highly nonlocal streamwise influence of $\partial V_1/\partial x_1$ on $\overline{u_2'v_1'}$. We qualitatively expect this to impact flows with an active streamwise gradient of the mean velocity, $\partial V_1/\partial x_1$, such as a spatially developing boundary layer. We also quantified differences in the streamwise extent of the eddy viscosity between various components of the Reynolds stresses. Reynolds stress transport models can incorporate anisotropy, and the observed anisotropy between the eddy viscosity kernels for various components of the Reynolds stress tensor can be used to quantitatively guide the modeling of the turbulence lengthscales or timescales.

APPENDIX A: DERIVATION OF THE RELATIONSHIP BETWEEN $\mathcal{L}$ AND $\overline{\mathcal{L}}$

The derivation for the relation in Eq. (10) is reproduced from Mani and Park [8] below. The governing equations, such as the GMT equations in Eqs. (3a) and (3b), can be written as

$$\mathcal{L}v = s, \tag{A1}$$

where v is a vector of velocity and pressure, $\mathcal{L}$ is a linear operator, and s is the MFM forcing. Similarly, the averaged equations can be written as

$$\overline{\mathcal{L}}V = \overline{s}, \tag{A2}$$

where V is a vector of mean velocity and mean pressure, $\overline{\mathcal{L}}$ is a linear operator, and $\bar{s}$ is the MFM forcing. The averaged operator, $\overline{\mathcal{L}}$, is unknown, and a relation between $\overline{\mathcal{L}}$ and $\mathcal{L}$ is desired. Let averaging be defined by a projection operator, P, such that

$$V = Pv. \tag{A3}$$

While the MFM forcing satisfies the property $s = \bar{s}$, s and $\bar{s}$ may discretely have different dimensions; thus, let E be an extension operator such that

$$s = E\bar{s}. \tag{A4}$$

Rearranging Eq. (A1) and substituting into Eq. (A3) leads to

$$V = P\mathcal{L}^{-1}s = P\mathcal{L}^{-1}E\bar{s}, \tag{A5}$$

where the definition of the extension operator in Eq. (A4) is used. Further rearrangement,

$$(P\mathcal{L}^{-1}E)^{-1}V = \bar{s}, \tag{A6}$$

and comparison with Eq. (A2) leads to the relation for $\overline{\mathcal{L}}$ in Eq. (10).

APPENDIX B: ADJOINT MFM FOR SCALAR TRANSPORT

In this Appendix, we derive adjoint MFM for passive scalar transport. For passive scalar transport, the generalized eddy diffusivity is a second-order tensor rather than a fourth-order eddy viscosity tensor. As a simpler example than momentum transport, the derivation for passive scalar transport more clearly shows the transposition of the indices in the eddy diffusivity tensor.

Discretely, the forced scalar transport equation for a passive scalar c is

$$\mathcal{L}c = s, \tag{B1}$$

where

$$\mathcal{L} = \frac{\partial}{\partial t} + u_i \frac{\partial}{\partial x_i} - D_M \frac{\partial^2}{\partial x_i \partial x_i}, \tag{B2}$$

and where u_i is the velocity field from the Navier–Stokes equations in Eqs. (2a) and (2b) and D_M is molecular diffusivity. The mean scalar transport equation is

$$\overline{\mathcal{L}}\bar{c} = \bar{s}, \tag{B3}$$

where

$$\overline{\mathcal{L}} = \frac{\partial}{\partial t} + U_i \frac{\partial}{\partial x_i} - D_M \frac{\partial^2}{\partial x_i \partial x_i} + \overline{\mathcal{L}}', \tag{B4}$$

and where the closure operator is

$$\overline{\mathcal{L}}'\overline{c} = \frac{\partial}{\partial x_i}\overline{u_i'c'} = -\frac{\partial}{\partial x_i}D_{ij}\frac{\partial \overline{c}}{\partial x_j}, \tag{B5}$$

and D_{ij} is the discretized eddy diffusivity tensor. The above equation, written out as block matrices and vectors, is

$$\begin{bmatrix} \frac{\partial}{\partial x_1} & \frac{\partial}{\partial x_2} & \frac{\partial}{\partial x_3} \end{bmatrix} \begin{bmatrix} \overline{u_1'c'} \\ \overline{u_2'c'} \\ \overline{u_3'c'} \end{bmatrix} = -\begin{bmatrix} \frac{\partial}{\partial x_1} & \frac{\partial}{\partial x_2} & \frac{\partial}{\partial x_3} \end{bmatrix} \begin{bmatrix} D_{11} & D_{12} & D_{13} \\ D_{21} & D_{22} & D_{23} \\ D_{31} & D_{32} & D_{33} \end{bmatrix} \begin{bmatrix} \frac{\partial}{\partial x_1} \\ \frac{\partial}{\partial x_2} \\ \frac{\partial}{\partial x_3} \end{bmatrix} \overline{c}, \tag{B6}$$

where for each $i, j \in \{1, 2, 3\}$, $\partial/\partial x_i$ is a $N \times N$ block matrix, $\overline{u_i'c'}$ is a $N \times 1$ vector, D_{ij} is a $N \times N$ block matrix, $\overline{c}$ is a $N \times 1$ vector, and N is the number of degrees of freedom in the averaged space.

For adjoint MFM, we transpose $\overline{\mathcal{L}}'$ by transposing the operator on the right-hand side of Eq. (B6):

$$\overline{\mathcal{L}}^{\top\prime} = -\begin{bmatrix} \frac{\partial}{\partial x_1} & \frac{\partial}{\partial x_2} & \frac{\partial}{\partial x_3} \end{bmatrix} \begin{bmatrix} D_{11}^{\top} & D_{21}^{\top} & D_{31}^{\top} \\ D_{12}^{\top} & D_{22}^{\top} & D_{32}^{\top} \\ D_{13}^{\top} & D_{23}^{\top} & D_{33}^{\top} \end{bmatrix} \begin{bmatrix} \frac{\partial}{\partial x_1} \\ \frac{\partial}{\partial x_2} \\ \frac{\partial}{\partial x_3} \end{bmatrix}. \tag{B7}$$

The transpose notation $\top$ denotes the swapping of the rows and columns of each D_{ij} block matrix, e.g., continuously $D^{\top} = D(\mathbf{y}, \mathbf{x})$. We also use the property that with proper boundary conditions, the transpose of each $\partial/\partial x_i$ block matrix is $-\partial/\partial x_i$.

Using IMFM, we can computationally assess the eddy diffusivity operator in Eq. (B7) by solving

$$\mathcal{L}^{\top}c^{\dagger} = s^{\dagger}, \tag{B8}$$

where $\mathcal{L}^{\top}$ is the transpose of the governing scalar transport operator in Eq. (B2):

$$\mathcal{L}^{\top} = -\frac{\partial}{\partial t} - u_i\frac{\partial}{\partial x_i} - D_M\frac{\partial^2}{\partial x_i\partial x_i}. \tag{B9}$$

After relabeling time such that $T = t_f - t$, where t_f is the final time:

$$\mathcal{L}^{\top} = \frac{\partial}{\partial T} - u_i\frac{\partial}{\partial x_i} - D_M\frac{\partial^2}{\partial x_i\partial x_i}. \tag{B10}$$

The corresponding closure operator is thus

$$\overline{\mathcal{L}}^{\top\prime}\overline{c}^{\dagger} = -\frac{\partial}{\partial x_i}\overline{u_i'c^{\dagger\prime}} = -\frac{\partial}{\partial x_i}D_{ji}^{\top}\frac{\partial \overline{c}^{\dagger}}{\partial x_j}. \tag{B11}$$

Using IMFM, we force elements of the adjoint mean scalar gradient and post-process the adjoint scalar flux to obtain columns of $D_{ji}^{\top}$. Continuously,

$$\overline{u_j'c^{\dagger\prime}}(\mathbf{y}, \tau) = \int_{\mathbf{x},t} D_{ij}(\mathbf{x}, \mathbf{y}, t, \tau)\frac{\partial \overline{c}^{\dagger}}{\partial x_i}\bigg|_{\mathbf{x},t} d\mathbf{x}dt, \tag{B12}$$

where we have relabeled the indices $i \leftrightarrow j$ and the coordinates $\mathbf{x} \leftrightarrow \mathbf{y}$ and $t \leftrightarrow \tau$.

APPENDIX C: ROW VERSUS COLUMN COMPARISON FOR D_{ij21} FOR THE 1D WALL-NORMAL EDDY VISCOSITY

In general, the rows of the eddy viscosity are not identical to the columns. Figure 3 showed the asymmetry in row versus column for D_{2121} at $x_2 = -0.565$. Figure 16 shows the asymmetry in row versus column for other components of D_{ij21} at $x_2 = -0.565$. Adjoint MFM results from Fig. 5 are also plotted for comparison.
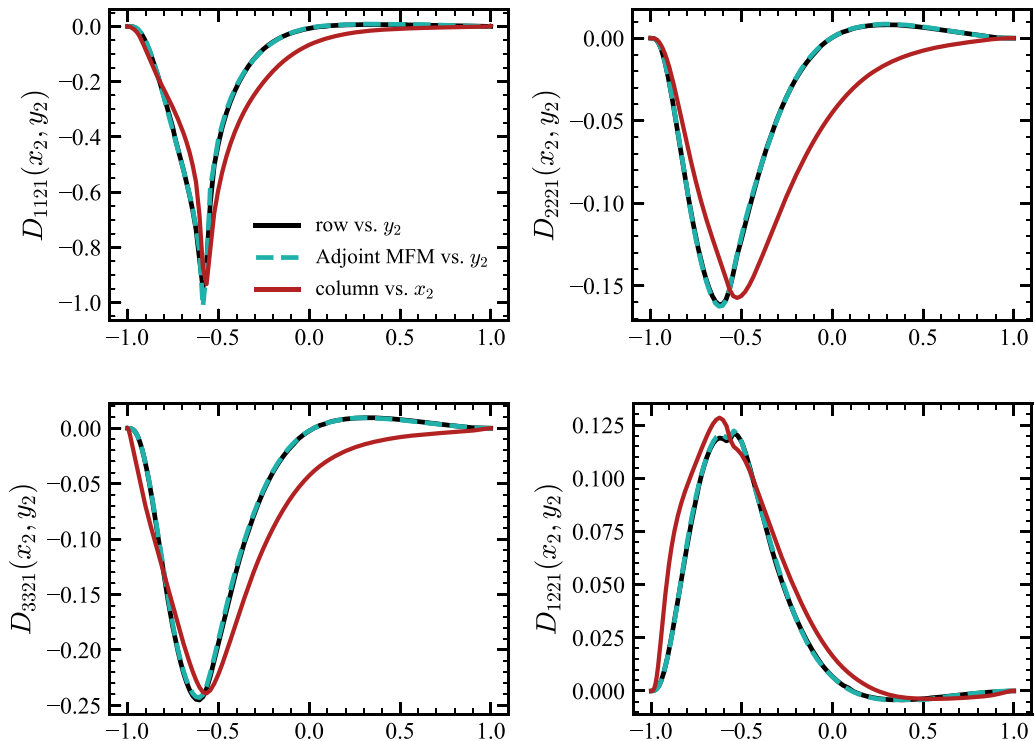
FIG. 16. Comparison of row versus column for D_{ij21} components using data from Park and Mani [6]. The corresponding row computed using adjoint MFM is also shown.

APPENDIX D: REFINEMENT AND NUMERICAL SCHEME EFFECTS ON THE 2D NONLOCAL EDDY VISCOSITY

In this Appendix, we examine the effect of refinement and an upwinding scheme on the quantified eddy viscosity kernels, particularly on the observed numerical oscillations. For computational ease, we show the results for an eddy viscosity column from an MFM calculation rather than an eddy viscosity row from an adjoint MFM calculation; however, we expect the effects of refinement and numerical scheme to be qualitatively similar between the two cases. Section V C 2 discusses differences between 2D eddy viscosity columns and rows.

Figure 17 shows a column of the eddy viscosity, $D_{2121}(x_2, y_1 - x_1, y_2)$ at $y_2 = -0.946$, similar to Fig. 9 but with a box size of $L_1 = 2\pi$ for computational ease. The mesh is uniform in the x_1 direction with $N_1 = 144$ grid points. This is identical to the box size and grid resolution of Park and Mani [6] for using MFM to compute the 1D wall-normal eddy viscosity. Figure 17 also shows the same column of the eddy viscosity under mesh refinement with $N_1 = 288$. While refinement in the x_1 direction reduces the numerical oscillations, it does not eliminate them. As was discussed in Sec. V C 1, the thin region that needs to be resolved due to the Dirac δ function source term is proportional to ν/U_1 and would require a much finer resolution. Figure 18(a) shows the eddy viscosity column integrated over the wall-normal direction, where the impact of refinement on the numerical oscillations is more clearly visible. Other than the oscillations, the overall shape of the kernel is unchanged with refinement.

Figure 17 also shows the same column of the eddy viscosity with an upwind scheme used for the streamwise advection of v_i in the GMT equation in Eq. (3a). The central differences schemes for all of the other terms in the GMT equations in Eqs. (3a) and (3b) and all terms in the Navier–Stokes equations in Eqs. (2a) and (2b) are unchanged. The upwind scheme completely removes the
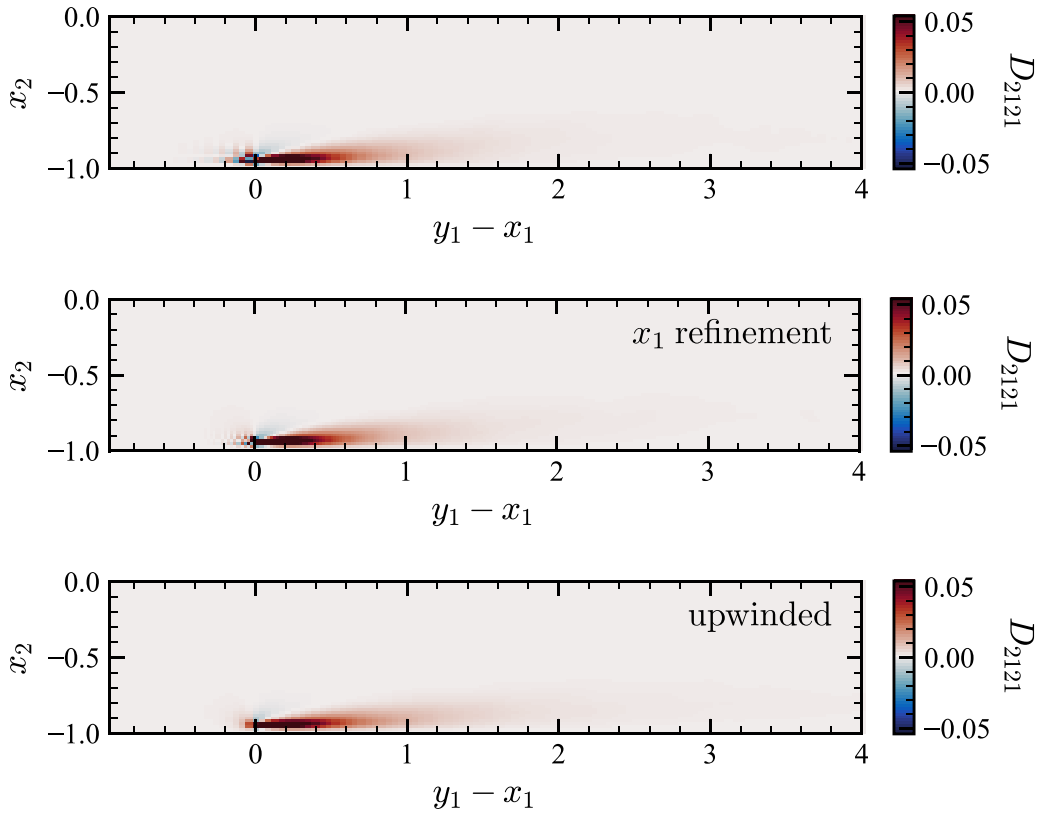
FIG. 17. Comparison of $D_{2121}(x_2, y_1 - x_1, y_2 = -0.946)$ (column). The top plot shows the original kernel, the middle plot shows the kernel with mesh refinement in x_1, and the bottom plot shows the effect of upwinding the streamwise advection in the GMT equation.
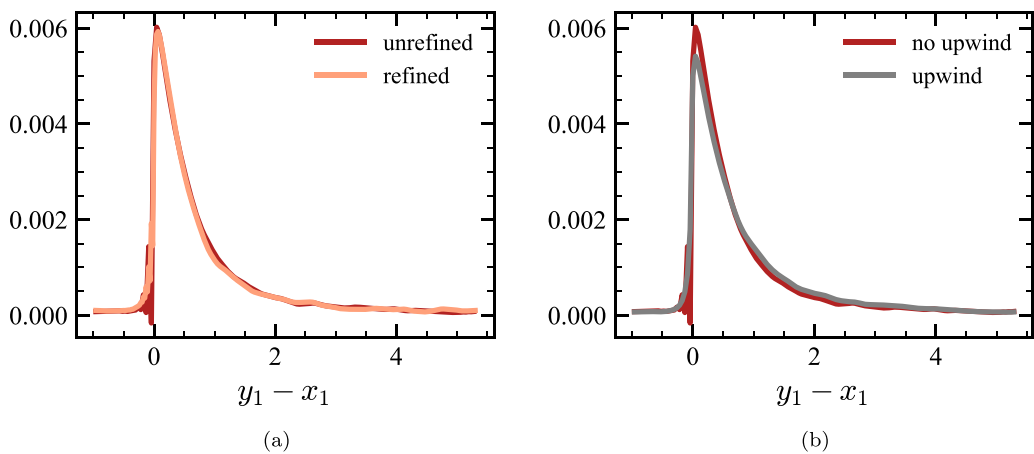

FIG. 18. Comparison of the effect of (a) mesh refinement in x_1 or (b) an upwind scheme on the streamwise column, computed by integrating the 2D kernels in Fig. 17 over the x_2 direction.

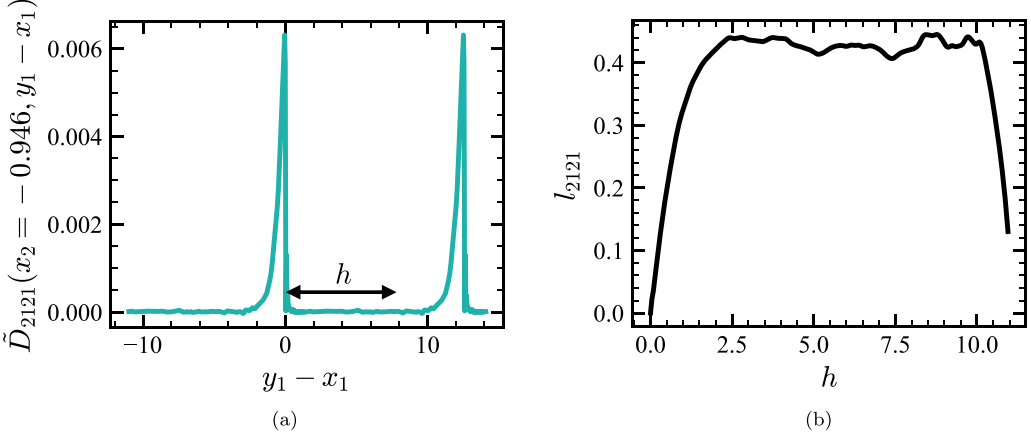FIG. 19. (a) Streamwise dependence of the wall-normal integrated eddy viscosity kernel at $x_2 = -0.946$. (b) $l_{2121} = -D_{2121}^{1_s}/D_{2121}^{0}$ at $x_2 = -0.946$ as a function of the the integration limits, $\eta = -h$ to $\eta = h$, where $\eta = y_1 - x_1$. The lengthscale is computed based on the flat region where the integration limits have little effect on l_{2121}.

oscillations; however, the additional numerical diffusion caused by the upwind scheme also smooths out the kernel's overall shape and reduces the peak. The difference is seen more clearly when the eddy viscosity column is integrated over the wall-normal direction, as shown in Fig. 18(b). Hence, we do not use an upwind scheme as it changes the shape of the eddy viscosity kernel.

APPENDIX E: DETAILS FOR COMPUTING THE STREAMWISE NONLOCALITY LENGTHSCALE

In this Appendix, we include details for computing the streamwise nonlocality lengthscale, $l_{2121} = -D_{2121}^{1_s}/D_{2121}^{0}$, introduced in Sec. V C 3. Careful treatment of the streamwise integral is needed to handle domain effects from the periodic x_1 direction. Specifically, small but nonzero values in the tails of the eddy viscosity kernels are heavily weighted by the distance from the peak in the calculation of the first streamwise moment:

$$D_{2121}^{1_s}(x_2) = \iint (y_1 - x_1) D_{2121}(x_2, y_1 - x_1, y_2) dy_1 dy_2. \tag{E1}$$

For example, Fig. 19(a) shows the streamwise eddy viscosity kernel after integration over the wall-normal direction at $x_2 = -0.946$:

$$\tilde{D}_{2121}(x_2, y_1 - x_1) = \int D_{2121}(x_2, y_1 - x_1, y_2) dy_2. \tag{E2}$$

The streamwise eddy viscosity is periodically repeated to illustrate simulation domain effects. Ideally, $D_{2121}^{1_s}$ is calculated for an infinite domain in the x_1 direction. However, due to a finite domain and periodic box effects in the simulations, the streamwise eddy viscosity does not go exactly to zero [e.g., the mean value between $-10 \leqslant y_1 - x_1 \leqslant -5$ is about 1×10^{-5} in Fig. 19(a)]. These nonzero values in the tails of the eddy viscosity kernels are weighted by $y_1 - x_1$ in the calculation of $D_{2121}^{1_s}$ and thus have a larger effect on $D_{2121}^{1_s}$ than on D_{2121}^{0}. The integration limits become important for calculating $D_{2121}^{1_s}$. With asymmetric integration limits, e.g., $-10 \leqslant y_1 - x_1 \leqslant 3$, the nonzero values

skew the centroid to the left. Hence, we integrate symmetrically from $\eta = -h$ to $\eta = h$, where $\eta \equiv y_1 - x_1$, and plot $l_{2121} = -D_{2121}^{1_s}/D_{2121}^0$, as a function of the integration limits, $\pm h$, where

$$D_{2121}^{1_s}(x_2) = \int_{-1}^{1} \int_{\eta=-h}^{\eta=h} \eta D_{2121}(x_2, \eta, y_2) d\eta dy_2, \tag{E3a}$$

$$D_{2121}^0(x_2) = \int_{-1}^{1} \int_{\eta=-h}^{\eta=h} D_{2121}(x_2, \eta, y_2) d\eta dy_2. \tag{E3b}$$

Figure 19(b) shows a flat region in l_{2121} versus h where the integration limits have little effect on l_{2121}. We use the average in this region, $3 \leqslant h \leqslant 9$, as the streamwise nonlocality lengthscale estimate, l_{2121}. For $x_2 = -0.946$, the streamwise nonlocality lengthscale is $l_{2121} = 0.42$.

APPENDIX F: PERIODIC DOMAIN EFFECTS ON THE 2D NONLOCAL EDDY VISCOSITY

In this Appendix, we investigate domain size effects on the 2D nonlocal eddy viscosity due to periodic boundary conditions in the x_1 direction. In the limit of an infinite domain, we expect the eddy viscosity kernel to go to zero very far away from the forcing location. The D_{3321} component in Fig. 20, shows slight wraparound of the eddy viscosity due to the periodic boundary conditions. Rather than a longer domain, which is computationally more expensive, we show a comparison with the shorter domain, e.g., used by Park and Mani [6] for their 1D wall-normal eddy viscosity calculations, to gain a qualitative understanding of the effect of periodic boundary conditions and a truncated domain.

Figure 20 shows a comparison between a domain size of $L_1 = 4\pi$, the domain size used for Fig. 15, and $L_1 = 2\pi$, the domain size used by Park and Mani [6]. The color bar for both plots is truncated to the same maximum color bar values as Fig. 15. While the qualitative shape of the eddy viscosity is unaffected by the domain size, the eddy viscosity is more negative for the $L_1 = 2\pi$ domain than the $L_1 = 4\pi$ domain due to wraparound from the periodic boundary condition. Figure 21 shows the eddy viscosity kernels in Figure 20 integrated over the wall-normal direction, where the negative shift due to the periodic boundary condition is more apparent. Periodic superposition of the eddy viscosity kernel integrated over the wall-normal direction for the $L_1 = 4\pi$ domain approximately results in the eddy viscosity kernel for the $L_1 = 2\pi$ domain as shown in Fig. 22.
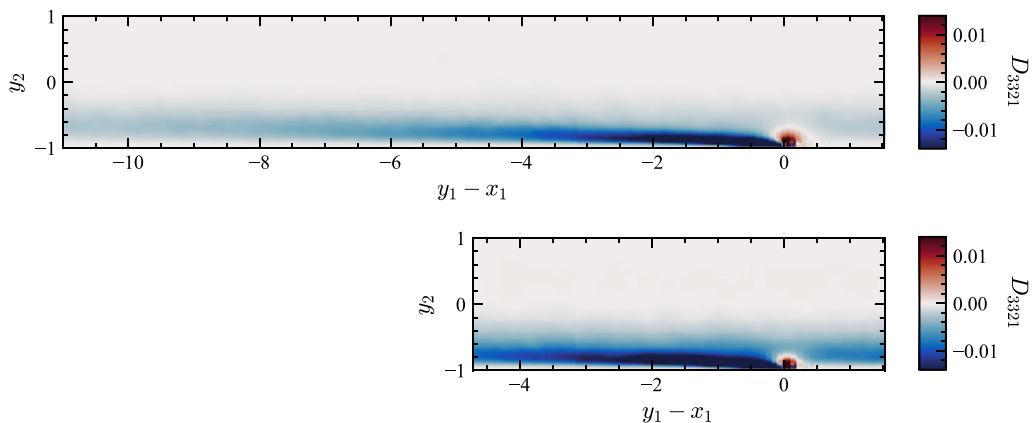

FIG. 20. Comparison of domain size effects on the D_{3321} component of the 2D eddy viscosity, corresponding to $\overline{u_3' v_3'}$, at $x_2 = -0.946$ ($x_2^+ \approx 10$). Top: $L_1 = 4\pi$; bottom: $L_1 = 2\pi$.
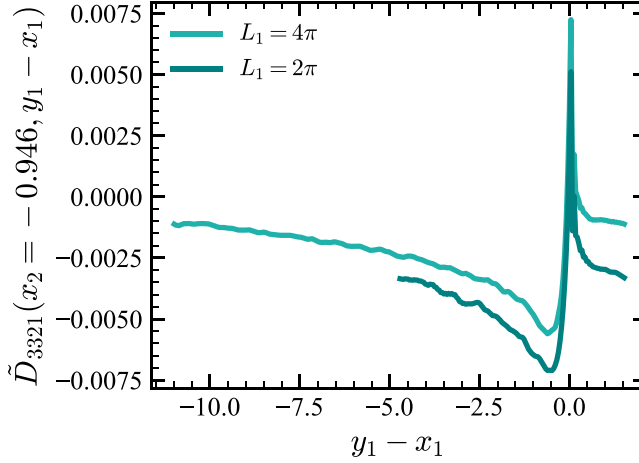
FIG. 21. Comparison of domain size effects on the $\tilde{D}_{3321}$ [tilde notation defined in Eq. (E2)] of the streamwise eddy viscosity, corresponding to the 2D eddy viscosity kernels in Fig. 20 integrated over the wall-normal direction.
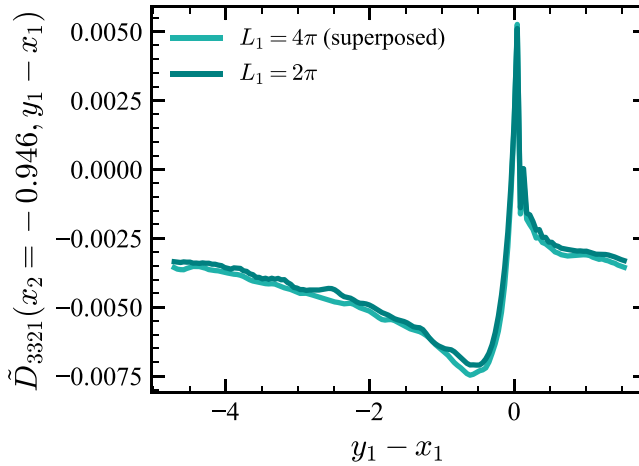

FIG. 22. Periodic superposition of the streamwise eddy viscosity kernel, $\tilde{D}_{3321}$, for the $L_1 = 4\pi$ domain approximately reproduces $\tilde{D}_{3321}$ for $L_1 = 2\pi$. In other words, the region from $-11 \leqslant y_1 - x_1 \leqslant -4.7$ for $L_1 = 4\pi$ in Fig. 21 is summed with the region from $-4.7 \leqslant y_1 - x_1 \leqslant 1.5$.

[1] S. B. Pope, *Turbulent Flows* (Cambridge University Press, Cambridge, UK, 2000).
[2] P. Spalart and S. Allmaras, A one-equation turbulence model for aerodynamic flows, in *Proceedings of the 30th Aerospace Sciences Meeting and Exhibit* (AIAA, Reno, NV, 1992), p. 439.
[3] F. R. Menter, Two-equation eddy-viscosity turbulence models for engineering applications, AIAA J. **32**, 1598 (1994).
[4] D. C. Wilcox, *Turbulence Modeling for CFD* (DCW Industries, La Canada, CA, 1998), Vol. 2.
[5] F. Hamba, Nonlocal analysis of the Reynolds stress in turbulent shear flow, Phys. Fluids **17**, 115102 (2005).

[6] D. Park and A. Mani, Direct calculation of the eddy viscosity operator in turbulent channel flow at $\mathrm{Re}_\tau = 180$, arXiv:2108.10898.

[7] R. H. Kraichnan, Eddy viscosity and diffusivity: Exact formulas and approximations, Complex Syst. **1**, 805 (1987).

[8] A. Mani and D. Park, Macroscopic forcing method: A tool for turbulence modeling and analysis of closures, Phys. Rev. Fluids **6**, 054607 (2021).

[9] J. Liu, H. H. Williams, and A. Mani, Systematic approach for modeling a nonlocal eddy diffusivity, Phys. Rev. Fluids **8**, 124501 (2023).

[10] D. C. Jespersen, T. H. Pulliam, and M. L. Childs, OVERFLOW turbulence modeling resource validation results, Tech. Rep. ARC-E-DAA-TN35216 (2016).

[11] A. Probst, R. Radespiel, C. Wolf, T. Knopp, and D. Schwamborn, A comparison of detached-eddy simulation and Reynolds-stress modeling applied to the flow over a backward-facing step and an airfoil at stall, in *Proceedings of the 48th AIAA Aerospace Sciences Meeting including the New Horizons Forum and Aerospace Exposition* (AIAA, Orlando, FL, 2010), p. 920.

[12] D. Park, J. Liu, and A. Mani, Direct measurement of the eddy viscosity tensor in a canonical separated flow: What is the upper bound of accuracy for local Reynolds stress models? in *Proceedings of the AIAA SciTech 2022 Forum* (AIAA, San Diego, CA, 2022), p. 0940.

[13] F. Hamba, Nonlocal expression for scalar flux in turbulent shear flow, Phys. Fluids **16**, 1493 (2004).

[14] D. L. O.-L. Lavacot, J. Liu, H. Williams, B. E. Morgan, and A. Mani, Nonlocality of mean scalar transport in two-dimensional Rayleigh-Taylor instability using the macroscopic forcing method, J. Fluid Mech. **985**, A47 (2024).

[15] S. H. Bryngelson, K. Schmidmayer, and T. Colonius, A quantitative comparison of phase-averaged models for bubbly, cavitating flows, Int. J. Multiphase Flow **115**, 137 (2019).

[16] S. H. Bryngelson, F. Schäfer, J. Liu, and A. Mani, Fast macroscopic forcing method, J. Comput. Phys. **499**, 112721 (2024).

[17] F. Schäfer and H. Owhadi, Sparse recovery of elliptic solvers from matrix-vector products, SIAM J. Sci. Comput. **46**, A998 (2024).

[18] F. Hamba, An analysis of nonlocal scalar transport in the convective boundary layer using the Green's function, J. Atmos. Sci. **52**, 1084 (1995).

[19] J. Boussinesq, Essai sur la théorie des eaux courantes, in *Mémoires Présentés Par Divers Savants a l'Academie des Sciences de l'Institute National de France* (Impr. Nationale, Paris, France, 1877), Vol. XXIII.

[20] S. Corrsin, Limitations of gradient transport models in random walks and in turbulence, Adv. Geophys. **18**, 25 (1975).

[21] M. Wang, Q. Wang, and T. A. Zaki, Discrete adjoint of fractional-step incompressible Navier-Stokes solver in curvilinear coordinates and application to data assimilation, J. Comput. Phys. **396**, 427 (2019).

[22] M. Wang and T. A. Zaki, State estimation in turbulent channel flow from limited observations, J. Fluid Mech. **917**, A9 (2021).

[23] T. A. Zaki and M. Wang, From limited observations to the state of turbulence: Fundamental difficulties of flow reconstruction, Phys. Rev. Fluids **6**, 100501 (2021).

[24] Q. Wang, Y. Hasegawa, and T. A. Zaki, Spatial reconstruction of steady scalar sources from remote measurements in turbulent flow, J. Fluid Mech. **870**, 316 (2019).

[25] S. T. Bose, P. Moin, and D. You, Grid-independent large-eddy simulation using explicit filtering, Phys. Fluids **22**, 105103 (2010).

[26] J. Seo, R. García-Mayoral, and A. Mani, Pressure fluctuations and interfacial robustness in turbulent flows over superhydrophobic surfaces, J. Fluid Mech. **783**, 448 (2015).

[27] Q. Wang, M. Wang, and T. A. Zaki, What is observable from wall data in turbulent channel flow? J. Fluid Mech. **941**, A48 (2022).

[28] J. Kim and P. Moin, Application of a fractional-step method to incompressible Navier–Stokes equations, J. Comput. Phys. **59**, 308 (1985).

[29] Y. Morinishi, T. S. Lund, O. V. Vasilyev, and P. Moin, Fully conservative higher order finite difference schemes for incompressible flow, J. Comput. Phys. **143**, 90 (1998).

[30] Q. Wang, P. Moin, and G. Iaccarino, Minimal repetition dynamic checkpointing algorithm for unsteady adjoint calculation, SIAM J. Sci. Comput. **31**, 2549 (2009).

[31] M. F. Eggl and P. J. Schmid, A gradient-based framework for maximizing mixing in binary fluids, J. Comput. Phys. **368**, 131 (2018).

[32] D. Park, J. Liu, and A. Mani, Non-Boussinesq effects of eddy viscosity in a separated turbulent boundary layer, in *Proceedings of the 34th Symposium on Naval Hydrodynamics* (SNH, Washington, D.C., 2022).

[33] J. Kim, P. Moin, and R. Moser, Turbulence statistics in fully developed channel flow at low Reynolds number, J. Fluid Mech. **177**, 133 (1987).

[34] B. E. Launder, G. J. Reece, and W. Rodi, Progress in the development of a Reynolds-stress turbulence closure, J. Fluid Mech. **68**, 537 (1975).

[35] C. G. Speziale, S. Sarkar, and T. B. Gatski, Modelling the pressure–strain correlation of turbulence: An invariant dynamical systems approach, J. Fluid Mech. **227**, 245 (1991).

[36] See Supplemental Material at http://link.aps.org/supplemental/10.1103/PhysRevFluids.9.094606 for the data files for the 2D streamwise and wall-normal eddy viscosity kernels shown in Figs. 8, 9, 10, 13, 14, and 15.